

The properties of the interstellar medium of galaxies across time as traced by the neutral atomic carbon [C I]

FRANCESCO VALENTINO,^{1,2} GEORGIOS E. MAGDIS,^{1,2,3,4} EMANUELE DADDI,⁵ DAIZHONG LIU,⁶ MANUEL ARAVENA,⁷
FRÉDÉRIC BOURNAUD,⁵ ISABELLA CORTZEN,^{1,2} YU GAO,⁸ SHUOWEN JIN,^{9,10} STÉPHANIE JUNEAU,¹¹
JEYHAN S. KARTALTEPE,¹² VASILY KOKOREV,^{1,2} MIN-YOUNG LEE,^{13,14} SUZANNE C. MADDEN,⁵ DESIKA NARAYANAN,^{1,15,16}
GERGÖ POPPING,¹⁷ AND ANNAGRAZIA PUGLISI⁵

¹*Cosmic Dawn Center (DAWN)*

²*Niels Bohr Institute, University of Copenhagen, Lyngbyvej 2, DK-2100 Copenhagen Ø*

³*DTU-Space, Technical University of Denmark, Elektrovej 327, DK-2800 Kgs. Lyngby*

⁴*Institute for Astronomy, Astrophysics, Space Applications and Remote Sensing, National Observatory of Athens, GR-15236 Athens, Greece*

⁵*Laboratoire AIM-Paris-Saclay, CEA/DSM-CNRS-Université Paris Diderot, Irfu/Service d'Astrophysique, CEA Saclay, Orme des Merisiers, F-91191 Gif sur Yvette, France*

⁶*Max Planck Institute for Astronomy, Königstuhl 17, D-69117 Heidelberg, Germany*

⁷*Núcleo de Astronomía, Facultad de Ingeniería y Ciencias, Universidad Diego Portales, Av. Ejército 441, Santiago, Chile*

⁸*Purple Mountain Observatory & Key Laboratory for Radio Astronomy, Chinese Academy of Sciences, 10 Yuanhua Road, Nanjing 210033, People's Republic of China*

⁹*Instituto de Astrofísica de Canarias (IAC), E-38205 La Laguna, Tenerife, Spain*

¹⁰*Universidad de La Laguna, Dpto. Astrofísica, E-38206 La Laguna, Tenerife, Spain*

¹¹*National Optical Astronomy Observatory, 950 North Cherry Avenue, Tucson, AZ 85719, USA*

¹²*School of Physics and Astronomy, Rochester Institute of Technology, 84 Lomb Memorial Drive, Rochester NY 14623, USA*

¹³*Korea Astronomy and Space Science Institute, 776 Daedeokdae-ro, 34055 Daejeon, Republic of Korea*

¹⁴*Max-Planck-Institut für Radioastronomie, Auf dem Hügel 69, 53121 Bonn, Germany*

¹⁵*Department of Astronomy, University of Florida, 211 Bryant Space Sciences Center, Gainesville, FL 32611 USA*

¹⁶*University of Florida Informatics Institute, 432 Newell Drive, CISE Bldg E251, Gainesville, FL 32611*

¹⁷*European Southern Observatory, Karl-Schwarzschild-Strasse 2, D-85745, Garching, Germany*

(Received 2019; Revised 2019)

Submitted to ApJ

ABSTRACT

We report ALMA observations of the neutral atomic carbon transitions [C I] and multiple CO lines in a sample of ~ 30 main sequence galaxies at $z \sim 1$, including novel information on [C I] ($^3P_2 - ^3P_1$) and CO ($7 - 6$) for 7 of such normal objects. We complement our observations with a collection of > 200 galaxies with coverage of similar transitions, spanning the $z = 0 - 4$ redshift interval and a variety of ambient conditions from local to high-redshift starbursts. We find systematic variations in the [C I]/IR and [C I]/high- J_{upper} ($J_{\text{upper}} = 7$) CO luminosity ratios among the various samples. We interpret these differences as increased dense molecular gas fractions and star formation efficiencies in the strongest high-redshift starbursts with respect to normal main sequence galaxies. We further report constant $L'_{[\text{C I}]^3P_2 - ^3P_1} / L'_{[\text{C I}]^3P_1 - ^3P_0}$ ratios across the galaxy populations and redshifts, suggesting that gas temperatures T_{exc} traced by [C I] do not strongly vary. We find only a mild correlation with T_{dust} and that, generally, $T_{\text{exc}} \lesssim T_{\text{dust}}$. We fit the line ratios with classical photodissociation region models, retrieving consistently larger densities and intensities of the UV radiation fields in sub-mm galaxies than in main sequence and local objects. However, these simple models fall short in representing the complexity of a multi-phase interstellar medium and should be treated with caution. Finally, we compare our observations with the Santa Cruz semi-analytical model of galaxy evolution, recently

extended to simulate sub-mm emission. While we confirm the success in reproducing the CO lines, we find systematically larger [C I] luminosities at fixed IR luminosity than predicted theoretically. This highlights the necessity of improving our understanding of the mechanisms regulating the [C I] emission on galactic scales. We release our data compilation to the community.

Keywords: Galaxies: evolution, ISM, star formation, high-redshift — Submillimeter: galaxies, ISM

1. INTRODUCTION

An accurate description of the physical mechanisms regulating gas in galaxies is paramount to reach a complete understanding of how these systems evolve with cosmic time. The recent advent of powerful interferometers such as the Northern Extended Millimeter Array (NOEMA) and, especially, the Atacama Large Millimeter Array (ALMA) have played a major role in this regard, opening a window not only on traditional molecular gas tracers, such as ^{12}CO and dust (e.g., Magdis et al. 2012a; Carilli & Walter 2013; Bolatto et al. 2013; Scoville et al. 2014) in large samples of distant galaxies, but also on lines previously inaccessible because of their intrinsic faintness. These facilities have also allowed the study of galaxies at unprecedented redshifts and those representative of the bulk of the population, in addition to the extremely bright starbursts and sub-mm galaxies (SMGs). Particular attention has been given to alternative proxies for the total molecular gas mass in galaxies, highly desirable to complement CO and dust and to break the known degeneracies hampering these tracers (Zanella et al. 2018; Cortzen et al. 2019). However, multiple elements and molecules have now been detected in distant systems, allowing us to study their ionization conditions, chemistry, metallicity, densities and temperatures.

In a previous work (Valentino et al. 2018, V18 hereafter), we presented results on the lowest neutral carbon transition [C I]($^3P_1 - ^3P_0$) ($\nu_{\text{rest}} = 492.161$ GHz) in normal galaxies at $z \sim 1.2$ that lie on the so called “main sequence” in the stellar mass - star formation rate plane (M_\star -SFR, Noeske et al. 2007; Elbaz et al. 2007; Daddi et al. 2007; Magdis et al. 2010; see also Bourne et al. 2019; Brisbin et al. 2019; Lamarche et al. 2019). The use of [C I] has theoretical and observational roots that have been deepened over the years, revealing potential advantages over alternative tracers (e.g., Papadopoulos et al. 2004, Madden et al. in prep.). In V18 we showed that [C I]($^3P_1 - ^3P_0$) and low- J CO line emissions correlate on global scales irrespectively of the redshift and galaxy type, bridging previous observations of local infrared (IR) luminous objects (e.g., Gerin & Phillips 2000; Papadopoulos et al. 2004; Liu et al. 2015; Israel et al. 2015; Kamenetzky et al. 2016; Jiao et al.

2017, 2019a) and high-redshift SMGs (Walter et al. 2011; Alaghband-Zadeh et al. 2013; Yang et al. 2017; Bothwell et al. 2017; Andreani et al. 2018; Cañameras et al. 2018; Nesvadba et al. 2018, to mention some recent efforts). Moreover, we reported systematic variations of the $L'_{[\text{C I}](^3P_1 - ^3P_0)}/L_{\text{IR}}$ luminosity ratio of normal main sequence galaxies from the starbursting SMG population, consistently with results based on CO (e.g., Daddi et al. 2010; Magdis et al. 2012b; Genzel et al. 2015; Tacconi et al. 2018), supporting the existence of different star formation regimes characterized by varying star formation efficiencies (SFE = SFR/ M_\star). This also resulted in different [C I] abundances in main sequence, starburst and SMG galaxies, naturally following the standard assumptions on the α_{CO} and dust-to-gas conversion factors.

Here we move from the ground we laid in our previous work (i) expanding our analysis to larger samples that became available during the last year, and (ii) simultaneously studying multiple line transitions, allowing us to study the properties of the interstellar medium across redshift and galaxy types. In particular, we introduce new ALMA observations of the excited [C I]($^3P_2 - ^3P_1$) line ($\nu_{\text{rest}} = 809.344$ GHz) in 30% of the main sequence galaxies that we presented in V18, giving simultaneous access to the CO (7 – 6) transition. These observations open a view both on the excited [C I] gas, allowing for a direct estimate of the gas temperature via the [C I]($^3P_2 - ^3P_1$)/[C I]($^3P_1 - ^3P_0$) ratio (Stutzki et al. 1997; Schneider et al. 2003; Weiß et al. 2003; Papadopoulos et al. 2004), and on the dense and warm gas phases so far explored only in the brightest galaxies at high redshift (e.g., Yang et al. 2017; Cañameras et al. 2018; Apostolovski et al. 2019). The availability of multiple line ratios for sizable and controlled samples of high-redshift galaxies is also the basis for modeling the [C I], CO, and dust emission, a historically complicated endeavor especially for what concerns [C I]. Classical monodimensional photodissociation region models predict the [C I] emission to arise only from a thin layer in between [C II] and CO (Tielens & Hollenbach 1985; Kaufman et al. 1999), struggling to reproduce fully concomitant [C I] and CO emission in local giant molecular clouds (Keene et al. 1996; Ojha

et al. 2001; Ikeda et al. 2002). More recent refinement, including non-equilibrium chemistry (Stoerzer et al. 1997), turbulent mixing (Xie et al. 1995; Glover et al. 2015), clumpy geometries (Stutzki et al. 1998), and the effect of cosmic rays (Papadopoulos et al. 2004, 2018; Bisbas et al. 2015, 2017) and 3D geometry (Bisbas et al. 2012) have been more successful in this sense. The addition of extra heating mechanisms (e.g., shocks, Lee et al. 2019), or radically different approaches (e.g., large velocity gradients, LVG, Young & Scoville 1991) have been recently successful in reproducing the interstellar medium (ISM) conditions in local resolved star forming regions or CO+[C I] emission in nuclear starbursts (Israel et al. 2015), detecting multiple phases traced by different line transitions. However, such modeling requires large amount of data tracing the various ISM components, which become progressively hard to collect at increasing redshifts or for faint galaxies. A tradeoff between model complexity and its applicability is what we aim at in this work.

Finally, the availability of a large compilation of galaxies with [C I] detections allows one to insert this emission line in the cosmological context of galaxy evolution. Recent works have been focusing on the modeling of the CO and [C II] emission, given their intrinsic brightness and coverage up to extremely high redshift (see Olsen et al. 2018, and references therein for a recent review), reaping the first rewards of such effort. Less attention has been dedicated to [C I], but models are quickly filling the gap. Here we focus on a recent implementation of the sub-mm lines emission modeling onto the Santa Cruz semi-analytical model described in Popping et al. (2019a). We will show how the fiducial model compares with the observed [C I], CO, and IR luminosities and how these observables can be inserted in the empirical frame of known scaling relations across redshifts.

This paper is organized as follows. In Section 2, we present the new ALMA data targeting [C I]($^3P_2 - ^3P_1$)+CO(7-6) in main sequence galaxies at $z \sim 1.2$, along with the description of the data compilation we assembled from the literature. Section 3 includes the main observational results of our work and their interpretation in the frame of the empirical scaling relations. In Section 4, we apply a simple photodissociation region model to interpret the observed trends, we discuss its limitations, and we introduce the comparison with the semi-analytical modeling mentioned above. Section 5 summarizes the results of our work. The whole data compilation we assembled for this work is made publicly available in an electronic format in the online ver-

sion or by requesting it to the contact author. Unless stated otherwise, we assume a Λ CDM cosmology with $\Omega_m = 0.3$, $\Omega_\Lambda = 0.7$, and $H_0 = 70 \text{ km s}^{-1} \text{ Mpc}^{-1}$ and a Chabrier initial mass function (IMF, Chabrier 2003). All magnitudes are expressed in the AB system. All the literature data have been homogenized with our conventions.

2. SAMPLE AND OBSERVATIONS

The galaxies we study here largely overlap with the sample of main sequence galaxies presented in Valentino et al. (2018). In this work, we also present new observations of the [C I]($^3P_2 - ^3P_1$) and CO(7-6) transitions for 7 objects from V18 observed during ALMA Cycle 6. We further add the recent observations of main sequence galaxies by Bourne et al. (2019) and Popping et al. (2017), and the sub-mm galaxies listed in Yang et al. (2017); Andreani et al. (2018); Cañameras et al. (2018); Nesvadba et al. (2018); Dannerbauer et al. (2019); Jin et al. (2019). In total we retrieve information about [C I] emission in 217 galaxies¹. A certain degree of inhomogeneity is inherent in the nature of such a large literature compilation (e.g., different selections, single dish vs interferometric observations, flux extraction, modeling). Whenever possible, we homogenized the measurements adopting a single approach, for example when fitting the far-IR SED (see below, Appendix A, and the supplementary material). Here we briefly summarize the salient properties of each sample, referring the reader to Valentino et al. (2018) and the original papers for further details. Statistics of the data collection are reported in Table 1.

2.1. Main sequence galaxies

This sample is composed of two main sets of observations described in Valentino et al. (2018) and Bourne et al. (2019), plus a single object from Popping et al. (2017).

2.1.1. The [C I]($^3P_1 - ^3P_0$) transition

- **Valentino et al. (2018, V18)**: In our previous work, we selected 50 targets mainly lying on the upper main sequence at $z \sim 1.1 - 1.3$ in the COSMOS field (Scoville et al. 2007), while including a subsample of starburst galaxies (i.e., $> 3.5\times$ above the main sequence, Figure 1 in V18). The targets had available

¹ Our collection refers to published material prior to May 2019, to the best of our knowledge. Other works have been brought to our attention after we conducted our analysis (e.g., Gullberg et al. 2016; Strandet et al. 2017; Lelli et al. 2018; Man et al. 2019). These and further results will be included in future versions of this database.

Table 1. Statistics of the data compilation.

Reference	[C I](${}^3P_1 - {}^3P_0$)	[C I](${}^3P_2 - {}^3P_1$)	$J_{\text{upper}} < 3$	$3 \leq J_{\text{upper}} \leq 6$	$J_{\text{upper}} \geq 7$
High-redshift main sequence galaxies					
This work, Valentino et al. (2018)	20 (3)	7 (0)	11 (0)	19 (0)	7 (0)
Bourne et al. (2019)	6 (4)	4 (5)	...
Popping et al. (2017) ; Talia et al. (2018)	1 (0)	1 (0)	...
Total	27 (7)	7 (0)	11 (0)	24 (5)	7 (0)
Local IR-luminous galaxies					
Liu et al. (2015) ; Kamenetzky et al. (2016)[†]	32 (114)	126 (20)	29 (0)	56 (90)	104 (42)
High-redshift SMGs and QSOs					
Walter et al. (2011) ; Alaghband-Zadeh et al. (2013) ; Cortzen et al. (submitted)	17 (4)	11 (7)	...	22 (0)	12 (1)
Bothwell et al. (2017)	9 (4)	...	9 (0)	13 (0)	...
Cañameras et al. (2018) ; Nesvadba et al. (2018) ; Harrington et al. (2018)	7 (0)	8 (0)	5 (0)	11 (0)	10 (0)
Yang et al. (2017) ; Andreani et al. (2018)	...	7 (4)	...	11 (0)	10 (1)
Dannerbauer et al. (2019)	1 (0)	...	1 (0)	1 (0)	...
Jin et al. (2019)	1 (0)	1 (0)	...
Total	35 (8)	26 (11)	15 (0)	59 (0)	32 (1)

NOTE—Line coverage: 3σ detections (upper limits).

[†]: The mid- and high- J CO measurements refer only to the CO (4–3) and CO (7–6) that we investigated here. See [Liu et al. \(2015\)](#) for results concerning the remaining CO transitions.

stellar mass estimates ([Muzzin et al. 2013](#); [Laigle et al. 2016](#)), a spectroscopic confirmation from the COSMOS master catalog (M. Salvato et al. in preparation.), and a *Herschel*/PACS 100 μm and/or 160 μm 3σ detection in the PEP catalog ([Lutz et al. 2011](#)). These galaxies were followed up in ALMA Band 6 during Cycle 4 (Project ID: 2016.1.01040.S, PI: F. Valentino), covering [C I](${}^3P_1 - {}^3P_0$) and, for part of the sample, CO (4–3). The ALMA campaign resulted in a secure determination of 18 detections and 3 upper limits on [C I](${}^3P_1 - {}^3P_0$) down to an average rms per beam of $\sim 0.15 \text{ Jy km s}^{-1}$ for a line width of 400 km s^{-1} . We computed the upper limits as $I < 3 \times \text{rms}_{\text{ch}} \sqrt{\Delta V dv}$, where rms_{ch} is the average noise per channel over the velocity range ΔV of other securely detected lines for each individual source, and dv is the velocity bin size in km s^{-1} (see, e.g., Eq. 7 of [Bothwell et al. 2013](#)). Here we add two extra sources from that sample with secure [C I](${}^3P_1 - {}^3P_0$) detections, but excluded from V18 be-

cause of the absence of a second sub-mm transition to confirm the redshift, now granted by [C I](${}^3P_2 - {}^3P_1$) and CO (7–6) (Section 2.1.2). Furthermore, all 14 galaxies with CO (4–3) coverage have been detected during the same runs. Moreover, 15 and 11 galaxies have CO (5–4) and CO (2–1) detections as part of independent ALMA programs (Project IDs: 2015.1.00260.S, 2016.1.00171.S, PI: Daddi; E. Daddi et al. 2019, in preparation). A large fraction of this sample (19/23) is also detected in the 1.1 and/or 3 mm continuum emission. We modeled the latter together with the whole far-IR SEDs listed in the “super-deblended” COSMOS catalog ([Jin et al. 2018](#)) following the prescriptions of [Magdis et al. \(2012b\)](#). We adopted the expanded [Draine & Li \(2007\)](#) models and incorporated the AGN templates by [Mullaney et al. \(2011\)](#) to derive and subtract the contribution of dusty tori to the integrated 8–1000 μm IR luminosity, L_{IR} , for every source in the sample. Moreover, we flag as “AGN” objects with at least a 1/3

contribution to the total L_{IR} from an active nucleus, whose $L_{\text{IR,AGN}}$ is detected with $S/N > 10$. We cross-checked this selection against the IRAC color criterion by Donley et al. (2012), retrieving consistent results. We note that our decomposition is sensitive to the coverage of the mid-IR wavelength regime and that it is effective to retrieve relatively bright AGN. We further remark that the detection of a millimeter continuum in the Rayleigh-Jeans tail of the dust emission is critical for a secure determination of the dust mass (e.g., Magdis et al. 2012b; Scoville et al. 2014). Finally, we estimated a luminosity-weighted dust temperature, T_{dust} , by fitting a modified black body model (MBB) to the SED. We report the line measurements for this sample in Table 2.

- **Bourne et al. (2019)** presented a set of 10 main sequence galaxies, selected from the Ultra Deep Survey (UDS) and in the COSMOS fields based on a SCUBA2 450 μm detection in the SCUBA2 Cosmology Legacy Survey (S2CLS; Geach et al. 2017). The sample covers the redshift range $z \sim 0.9 - 1.3$ as determined by the available *Hubble Space Telescope*/WFC3 G141 grism spectroscopy (Momcheva et al. 2016). All galaxies have a stellar mass determination (Skelton et al. 2014) and they have been followed up in ALMA band 6 during Cycle 4 and 5 (Project IDs: 2016.1.01184.S and 2017.A.00013.S PI: N. Bourne). The observations resulted in the detection of $[\text{C I}](^3P_1 - ^3P_0)$ at $> 3\sigma$ in 6/10 galaxies, a marginal measurement at $2 < \sigma < 3$ in 3/10 and an upper limit on 1/10 sources. $\text{CO}(4-3)$ measurements at $> 4\sigma$ are reported for 4/9 galaxies with proper physical coverage, along with 2/9 marginal detections at $2 < \sigma < 3$, and 3 upper limits. Continuum emission at ~ 1.1 mm is detected for 7/10 galaxies. In order to avoid systematics on L_{IR} and the dust mass, M_{dust} , purely due to modeling, we refitted the deblended far-IR SED (Bourne et al. 2017, 2019) using the same prescriptions reported in the previous paragraph. This resulted in ~ 0.2 dex larger M_{dust} and < 0.1 dex larger L_{IR} than originally listed in Bourne et al. (2019), consistently with well known systematics (Magdis et al. 2012b, V18).

- **Popping et al. (2017); Talia et al. (2018)**: Finally, we included the compact main sequence galaxy GS30274 at $z = 2.225$ reported in Popping et al. (2017) and subsequently followed up by Talia et al. (2018). This object has been selected in GOODS-South following criteria comparable with the ones in V18 (spectroscopic confirmation, detection in *Herschel*/PACS and SPIRE), but further requiring “compactness” (van Dokkum et al. 2015). This extra criterion results in starburst-like behavior of some properties (Popping

et al. 2017; Gómez-Guijarro et al. 2019), which put this object in a likely transitioning phase. GS30274 has been followed up in ALMA Bands 3 and 4 in Cycle 3 (Project ID: 2015.1.00228.S, PI: G. Popping), resulting in $> 10\sigma$ detections of $[\text{C I}](^3P_1 - ^3P_0)$ $\text{CO}(3-2)$, and $\text{CO}(4-3)$, along with a $> 6\sigma$ continuum emission at 2 mm. Talia et al. (2018) further reported Band 3 and 6 observations (Project ID: 2015.1.01379.S, PI: P. Cassata) and a $> 9\sigma$ detection of $\text{CO}(6-5)$ and the underlying 1.4 mm continuum at $> 5.5\sigma$ significance. Also in this case, we refit the SED following Magdis et al. (2012b), retrieving a $\sim 25\%$ AGN contribution to L_{IR} , consistent with the observed red IRAC colors (Donley et al. 2012) and the results in Talia et al. (2018). Correcting for the effect of the dusty torus, we find a 7% lower L_{IR} and a 2 \times larger M_{dust} than in Popping et al. (2017).

Altogether, we compiled 27 main sequence galaxies at $z \sim 0.9 - 2.2$ detected at $> 3\sigma$ in $[\text{C I}](^3P_1 - ^3P_0)$, plus 7 marginal detections or upper limits. Moreover, 24/34 sources have at least one detection of a mid- J CO transition ($J_{\text{upper}} = 3-5$), the rest of the sample having marginal measurements or upper limit on $\text{CO}(4-3)$ (5/34), $\text{CO}(5-4)$ (5/34) or not being covered at the relevant frequency ranges (1/34).

2.1.2. The $[\text{C I}](^3P_2 - ^3P_1)$ transition

During ALMA Cycle 6, we collected Band 7 observations for a set of 7 galaxies extracted from the sample in V18 (Project ID: 2018.1.00635.S, PI: F. Valentino). We selected the targets based on a secure $[\text{C I}](^3P_1 - ^3P_0)$ detection, the simultaneous observability of $[\text{C I}](^3P_2 - ^3P_1)$ and $\text{CO}(7-6)$, the availability of alternative line emissions ($\text{CO}(5-4)+\text{CO}(2-1)$) for 2/7 objects, $\text{CO}(5-4)$ only for 1/7), and a well constrained IR SED, allowing us to derive dust masses and total L_{IR} (Section 2.1.1). We selected 5 typical main sequence galaxies, 1 starburst, and 1 AGN. We targeted the $[\text{C I}](^3P_2 - ^3P_1)$ and $\text{CO}(7-6)$ lines within contiguous spectral windows of 1.875 GHz and with a spectral resolution of 7.8 MHz (~ 7 km s $^{-1}$), enough to spectrally resolve the emission lines. Five out of 7 targets were observed for the full proposed integration, the remaining being imaged for 75% of the initial request, resulting in a higher rms ($\#$ 35349 and 208273 in Table 3). Data were collected in the C43-1 configuration for a final synthesized beam of $\sim 0.9''$. We resolved the emission of every source, ensuring minimal flux losses with Gaussian extractions (Appendix B, Coogan et al. 2018; Puglisi et al. 2019). The data were reduced with a combination of the standard pipeline with CASA (McMullin et al. 2007) and a series of customized scripts

Table 2. Emission lines of main-sequence galaxies at $z \sim 1.2$.

ID	z_{spec}	L_{IR}	T_{dust}	$\langle U \rangle$	$L'_{[\text{C}]\text{I}^3 P_1 - 3 P_0}$	Units	$L'_{\text{CO}(2-1)}$	Units	$L'_{\text{CO}(4-3)}$	Units	$L'_{\text{CO}(5-4)}$	Units	$I_{[\text{C}]\text{I}^3 P_1 - 3 P_0}$	Units	$I_{\text{CO}(2-1)}$	Units	$I_{\text{CO}(4-3)}$	Units	$I_{\text{CO}(5-4)}$	Type
(1)	(2)	(3)	(4)	(5)	(6)	(7)	(8)	(9)	(10)	(11)	(12)	(13)	(14)	(15)	(16)	(17)	(18)	(19)	(20)	(21)
4233	1.1630 ± 0.0003	8.09 ± 0.49	27.8 ± 2.0	9.5 ± 2.5	0.24 ± 0.05	...	0.66 ± 0.07	< 0.21	0.60 ± 0.14	...	1.48 ± 0.15	< 0.74	MS							
7540	1.1714 ± 0.0003	9.36 ± 1.32	29.2 ± 1.4	8.5 ± 1.6	0.36 ± 0.08	...	0.65 ± 0.09	...	0.89 ± 0.20	...	1.42 ± 0.19	...	MS							
13205	1.2660 ± 0.0004	12.28 ± 1.27	40.0 ± 0.9	37.4 ± 5.0	< 0.21	2.10 ± 0.42	...	1.02 ± 0.09	< 0.45	0.99 ± 0.20	...	3.03 ± 0.27	MS							
13250	1.1484 ± 0.0002	5.22 ± 1.54	31.0 ± 5.0	14.2 ± 6.4	< 0.10	...	0.33 ± 0.04	< 0.10	< 0.27	...	0.74 ± 0.10	< 0.35	MS							
18538	1.2696 ± 0.0001	9.95 ± 0.62	34.2 ± 1.0	20.5 ± 3.4	0.23 ± 0.03	0.33 ± 0.05	< 0.51	0.96 ± 0.14	MS							
18911	1.1709 ± 0.0003	7.78 ± 1.68	40.4 ± 1.0	51.1 ± 7.1	< 0.20	...	0.81 ± 0.26	< 0.43	< 0.27	...	1.59 ± 0.40	< 1.47	MS							
19021	1.2581 ± 0.0003	19.27 ± 1.57	36.2 ± 0.7	23.9 ± 1.9	0.48 ± 0.09	1.90 ± 0.24	...	0.58 ± 0.03	1.06 ± 0.19	0.45 ± 0.14	...	1.73 ± 0.10	AGN							
26925	1.1671 ± 0.0003	9.13 ± 1.66	32.2 ± 1.3	15.0 ± 3.6	0.37 ± 0.07	1.47 ± 0.22	0.71 ± 0.08	< 0.20	0.93 ± 0.17	0.91 ± 0.12	1.58 ± 0.17	< 0.69	MS							
30694	1.1606 ± 0.0002	8.67 ± 1.45	33.2 ± 5.7	15.0 ± 4.6	0.24 ± 0.03	1.62 ± 0.21	0.48 ± 0.04	0.30 ± 0.04	0.61 ± 0.09	0.91 ± 0.12	1.07 ± 0.10	1.06 ± 0.14	MS							
32394	1.1345 ± 0.0001	22.54 ± 6.37	33.0 ± 1.8	20.5 ± 4.6	0.24 ± 0.05	...	0.58 ± 0.05	...	0.64 ± 0.12	...	1.37 ± 0.11	...	SB							
35349	1.2543 ± 0.0002	11.50 ± 1.83	27.6 ± 1.7	6.7 ± 2.5	0.41 ± 0.11	3.57 ± 0.44	...	0.45 ± 0.11	0.89 ± 0.25	1.72 ± 0.21	...	1.35 ± 0.33	MS							
36053	1.1573 ± 0.0003	7.99 ± 0.58	32.4 ± 1.4	17.0 ± 3.7	0.17 ± 0.05	...	0.44 ± 0.06	< 0.17	0.43 ± 0.13	...	1.00 ± 0.13	< 0.60	MS							
36945	1.1569 ± 0.0003	0.44 ± 0.03	36.8 ± 2.3	0.9 ± 0.1	0.17 ± 0.05	0.65 ± 0.26	0.35 ± 0.06	0.17 ± 0.05	0.44 ± 0.14	0.37 ± 0.15	0.79 ± 0.14	0.61 ± 0.16	AGN							
37250	1.1526 ± 0.0002	16.64 ± 0.62	30.4 ± 0.6	12.1 ± 1.2	0.68 ± 0.06	4.58 ± 0.32	...	0.84 ± 0.08	1.76 ± 0.16	2.60 ± 0.18	...	2.96 ± 0.30	MS							
37508	1.3020 ± 0.0003	11.20 ± 2.17	54.2 ± 2.3	81.2 ± 5.5	0.31 ± 0.08	0.49 ± 0.32	...	0.38 ± 0.06	0.64 ± 0.16	0.22 ± 0.14	...	1.06 ± 0.18	MS							
38053	1.1562 ± 0.0003	12.90 ± 4.03	37.2 ± 1.3	30.0 ± 5.8	0.27 ± 0.06	1.69 ± 0.31	0.60 ± 0.06	0.35 ± 0.08	0.69 ± 0.15	0.96 ± 0.17	1.34 ± 0.15	1.23 ± 0.27	SB							
44641	1.1495 ± 0.0002	9.19 ± 1.99	30.0 ± 0.7	10.0 ± 1.1	0.48 ± 0.07	1.63 ± 0.35	0.87 ± 0.08	0.27 ± 0.06	1.24 ± 0.17	0.93 ± 0.20	1.99 ± 0.17	0.95 ± 0.23	MS							
121546	1.1392 ± 0.0002	6.89 ± 0.94	32.8 ± 1.9	18.0 ± 4.9	0.47 ± 0.09	...	0.87 ± 0.15	...	1.24 ± 0.23	...	2.01 ± 0.34	...	MS							
188090	1.2364 ± 0.0003	28.97 ± 1.22	38.8 ± 0.4	25.0 ± 2.4	0.69 ± 0.13	1.56 ± 0.29	SB							
192337	1.2884 ± 0.0003	9.06 ± 0.64	33.2 ± 1.0	15.0 ± 2.2	0.30 ± 0.07	0.62 ± 0.14	MS							
208273	1.2662 ± 0.0003	4.25 ± 0.80	40.8 ± 8.5	50.0 ± 17.1	0.32 ± 0.07	0.69 ± 0.16	MS							
218445	1.1199 ± 0.0004	3.98 ± 1.07	24.8 ± 2.2	4.3 ± 2.4	0.49 ± 0.09	...	0.43 ± 0.09	...	1.33 ± 0.25	...	1.03 ± 0.22	...	MS							
256703	1.2740 ± 0.0002	7.05 ± 0.92	38.0 ± 3.0	32.8 ± 10.4	0.25 ± 0.06	0.53 ± 0.12	MS							

VALENTINO ET AL.

NOTE—Column 1: ID. Column 2: spectroscopic redshift. Column 3: total IR luminosity integrated within $8 - 1000 \mu\text{m}$. Column 4: dust temperature. Column 5: dust mass-weighted mean intensity of the radiation field for the *Draine & Li (2007)* models. Columns 6 to 9: galaxy-integrated $L'_{[\text{C}]\text{I}^3 P_1 - 3 P_0}$, $L'_{\text{CO}(2-1)}$, $L'_{\text{CO}(4-3)}$, and $L'_{\text{CO}(5-4)}$. Units: $10^{10} \text{ K km s}^{-1} \text{ pc}^2$. Columns 10 to 13: velocity integrated $[\text{C}]\text{I}^3 P_1 - 3 P_0$, CO (2 - 1), CO (4 - 3), and CO (5 - 4) fluxes. Column 14: galaxy type; MS = main-sequence; SB = starburst ($> 3.5 \times$ above the main-sequence); AGN = SED contaminated by torus emission. Upper limits at 3σ .

See *Valentino et al. (2018)* and Section 2.1.1 for details. (The data are available in the .fits files described in Table 6.)

Table 3. ALMA Band 7 observations of main-sequence galaxies at $z \sim 1.2$.

ID	$L'_{[\text{C I}]^3P_2 - ^3P_1}$ $10^{10} \text{ K km s}^{-1} \text{ pc}^2$	$L'_{\text{CO}(7-6)}$ $10^{10} \text{ K km s}^{-1} \text{ pc}^2$	$I_{[\text{C I}]^3P_2 - ^3P_1}$ Jy km s^{-1}	$I_{\text{CO}(7-6)}$ Jy km s^{-1}	S_{850} mJy
(1)	(2)	(3)	(4)	(5)	(6)
18538	0.11 ± 0.01	0.10 ± 0.01	0.63 ± 0.07	0.57 ± 0.07	1.20 ± 0.08
19021	0.25 ± 0.03	0.28 ± 0.02	1.45 ± 0.16	1.62 ± 0.14	2.38 ± 0.10
35349	0.09 ± 0.01	0.07 ± 0.01	0.53 ± 0.09	0.40 ± 0.07	1.86 ± 0.06
188090	0.38 ± 0.06	0.31 ± 0.06	2.29 ± 0.35	1.90 ± 0.35	3.50 ± 0.15
192337	0.14 ± 0.02	0.13 ± 0.02	0.80 ± 0.10	0.73 ± 0.11	1.16 ± 0.05
208273	0.09 ± 0.01	0.07 ± 0.01	0.54 ± 0.07	0.41 ± 0.07	0.71 ± 0.04
256703	0.15 ± 0.01	0.09 ± 0.01	0.87 ± 0.09	0.51 ± 0.08	1.16 ± 0.05

NOTE—See Table 2 for additional available transitions. Column 1: ID. Columns 2 and 3: galaxy-integrated $L'_{[\text{C I}]^3P_2 - ^3P_1}$ and $L'_{\text{CO}(7-6)}$ luminosities. Columns 4 and 5: velocity integrated $[\text{C I}]^3P_2 - ^3P_1$ and $\text{CO}(7-6)$ fluxes. Column 6: continuum emission flux density at $850 \mu\text{m}$.

(The data are available in the .fits files described in Table 6.)

with GILDAS² (Guiloteau & Lucas 2000), following the procedure described in V18 and Daddi et al. (2015). We consistently extracted 1D spectra for all the available lines, centering on the brightest peaks among all the transitions available. We scanned the 1D spectra and integrated the line fluxes over the number of channels maximizing the S/N ratio of each candidate line emission. These line fluxes were then increased by 10% to account for emission in extended wings as found by modeling the spectra with single or double Gaussian peaks. We performed such modeling using the χ^2 -minimization algorithm MPFIT (Markwardt 2009) and using both single and double Gaussians with constant velocity widths. In 6/7 cases the line emission are well fitted by double-peaked [C I]($^3P_2 - ^3P_1$) and CO (7 – 6) profiles. This resulted in a 100% detection rate of both transitions at $\gtrsim 6\sigma$. We measured line ratios by fixing the redshifts and line widths to the values for the highest S/N transitions among the ones available for each source, with the exception of #35349, for which the [C I]($^3P_2 - ^3P_1$) and CO (7 – 6) lines are wider than [C I]($^3P_1 - ^3P_0$) and CO (2 – 1). For the vast majority of our sources, the estimates are fully consistent with the ones reported in V18. In a few cases (notably #188090 and #35349) the results significantly varied based on the new [C I]($^3P_2 - ^3P_1$) and CO (7 – 6) broad line detections. We concurrently measured the continuum emission at observed $\sim 850 \mu\text{m}$ over 7.5 GHz assuming an intrinsic slope of $\nu = 3.7$ ($\beta = 1.7$), excluding the channels covered by the emission lines. We detected significant continuum emission at 15 – 30 σ in 7/7 sources.

All the line measurements and the underlying 850 μm continuum emission are reported in Table 3.

2.2. Local galaxies

- **Liu et al. (2015):** This sample is composed of galaxies from a compilation of *Herschel*/Fourier Transform Spectrometer (FTS) observations in the Herschel Science Archive of local galaxies. We retrieve 32 (126) objects with a [C I]($^3P_1 - ^3P_0$) ([C I]($^3P_2 - ^3P_1$)) detection at $> 3\sigma$. All 32 sources with a [C I]($^3P_1 - ^3P_0$) measurement are detected in [C I]($^3P_2 - ^3P_1$). Multiple $J_{\text{upper}} > 4$ CO lines are generally available (Liu et al. 2015). In particular, 31/32 sources with [C I]($^3P_1 - ^3P_0$) and 105/126 objects with [C I]($^3P_2 - ^3P_1$) have coverage of the CO (4 – 3) line (55 detections). All sources have coverage of CO (7 – 6) (104 detections). For consis-

tency, we checked our beam flux measurements against the independent analysis of Kamenetzky et al. (2016) and Israel et al. (2015), recovering consistent results for the sources in common among these samples. We corrected the $L_{\text{FIR}}(40 - 400 \mu\text{m})$ luminosities from *IRAS* Sanders et al. (2003) to L_{IR} by multiplying by a factor of $1.2\times$. This average correction was checked against full SED modeling for a subset of galaxies from the Great Observatories All-Sky LIRGs Survey (GOALS; Armus et al. 2009). For such subsample, we further estimated the dust temperature T_{dust} by fitting an MBB model as for the main sequence galaxies. As described in V18, we beam-matched the line luminosities to L_{IR} based on *Herschel*/PACS photometry. Therefore, the values adopted in our analysis refer to the total, galaxy-integrated quantities. We further include and beam-match the observations of low- J CO transitions from Kamenetzky et al. (2016). We finally checked for signatures of galaxy nuclear activity by cross-matching our sample with the catalog by Véron-Cetty & Véron (2010), retrieving 12/32 and 43/126 galaxies that we therefore flag as “active”. Given the observed luminosities and properties, the local galaxy sample is representative of the starbursting population, rather than typical low-redshift spirals (V18).

2.3. High-redshift Submillimeter Galaxies and Quasars

We collected information about recent observations of the [C I]($^3P_1 - ^3P_0$) and/or [C I]($^3P_2 - ^3P_1$) transitions in high-redshift SMGs and QSOs. For these objects, we retrieved the original far-IR to sub-mm SED and refitted it following the same procedure and adopting the identical models as for the main sequence galaxies in V18 described in the previous section. As noted in that paper, this general results in $\sim 1.5\times$ larger 8-1000 μm L_{IR} and up to $10\times$ larger M_{dust} than the widely adopted MBB law (e.g., Blain et al. 2003; Magdis et al. 2012b; Dale et al. 2012; Bianchi 2013). The difference is larger for sources particularly bright in the mid-IR (e.g., AGN/QSOs), where the difference between the MBB and the Draine & Li (2007) models is maximal. For the same reason, the more divergent the integration limits of the “far-IR” luminosities (L_{FIR} , 40-120 or 40-400 μm , depending on the convention) from the total L_{IR} (8-1000 μm), the greater the correction to apply. These differences are well known and entirely due to the adopted models and their parameters (effective dust emissivity index β , dust mass absorption coefficient κ , peak temperature; Magdis et al. 2012b). Only by correcting for these *systematic* deviations, we can safely compare the *relative* behavior of the various galaxy populations. We also notice that the vast majority of

² <http://www.iram.fr/IRAMFR/GILDAS>

galaxies in this sample does not have an estimate of the stellar mass and we cannot canonically define them as main sequence or starburst galaxies. However, their observed ISM conditions, gas and SFR densities, and SFEs generally distinguish SMGs from main galaxies, and we will thus consider them as starbursts as in our previous analysis (V18).

Altogether we collected information about 60 SMGs at $z \sim 2 - 5$, 35/60 detected in [C I](${}^3P_1 - {}^3P_0$) (8/60 upper limits) and 26/60 detected in [C I](${}^3P_2 - {}^3P_1$) (11/60 upper limits, Table 1). Moreover, 59/60 sources have at least one detection of a mid- J CO transition ($J_{\text{upper}} = 3 - 5$) and 21/60 are detected in CO (7 - 6) (4/60 upper limits).

- **Walter et al. (2011), Alaghband-Zadeh et al. (2013):** These authors targeted or collected information on typical 850 μm selected SMGs at $z \sim 2.5 - 4$, including a high-redshift tail of widely known and studied QSOs. Half of the sample is gravitationally magnified up to $\sim 30\times$ and 30% is contaminated or dominated by the emission of dusty tori surrounding the central supermassive black hole. Out of 23 galaxies, 17 are detected in [C I](${}^3P_1 - {}^3P_0$) and 11 in [C I](${}^3P_2 - {}^3P_1$) (10 galaxies have both lines available). Moreover, 4/23 and 7/23 objects have upper limits on [C I](${}^3P_1 - {}^3P_0$) and [C I](${}^3P_2 - {}^3P_1$), respectively. We notably substituted the old upper limits on the [C I] transitions in GN20 at $z = 4.055$ (Daddi et al. 2009; Casey et al. 2009) with the recent detections with the NOEMA interferometer (Cortzen et al., submitted). The vast majority of the sample (22/23) has a secure detection of CO (4 - 3) or CO (3 - 2) (5/23 galaxies have both line fluxes available). Moreover, 12/23 objects have a detection of CO (7 - 6) (1/23 upper limits). Sixty-five percent of these galaxies have interferometric observations.

- **Bothwell et al. (2017):** This sample comprises 13 strongly lensed systems ($\mu_{\text{magn}} \sim 3 - 30\times$) found in the 1.4 mm blank-field survey with the South Pole Telescope (SPT; Vieira et al. 2010; Weiß et al. 2013), spectroscopically confirmed to lie at $z = 3.3 - 4.8$ by multiple line transitions, including both high- and low- J CO transitions (Weiß et al. 2013; Aravena et al. 2016) and ionized carbon emission [C II] (Gullberg et al. 2015). Bothwell et al. (2017) reports [C I](${}^3P_1 - {}^3P_0$) ALMA detections at $> 3\sigma$ significance for 9/13 galaxies. No coverage of the [C I](${}^3P_2 - {}^3P_1$) line is available. Our SED modeling identifies only 1/13 source with a significant contribution ($f_{\text{AGN}} \sim 70\%$) of the central AGN to the total L_{IR} .

- **Cañameras et al. (2018); Nesvadba et al. (2018):** These authors report IRAM/EMIR single-dish observations of [C I](${}^3P_1 - {}^3P_0$) and/or [C I](${}^3P_2 - {}^3P_1$) in a subsample of 11 galaxies from the *Planck*'s dusty Gravitationally Enhanced subMillimetre Sources (GEMS; Cañameras et al. 2015). These objects have been initially selected as the brightest among the isolated, compact sources with the reddest 350 - 550 μm and 550 - 850 μm *Planck* colors and subsequently followed up with multiple facilities that sampled their far-IR / sub-mm SED and confirmed their redshift with several line transitions ($z = 2.2 - 3.5$, including CO (1 - 0) from Harrington et al. 2018). The magnification factor is generally well constrained both for the continuum and the line emission, spanning a range of $\mu_{\text{magn}} = 7 - 30\times$. When necessary, in the analysis we adopted separate μ_{dust} and μ_{gas} to correct the continuum emission and its derived properties (e.g., L_{IR} , M_{dust}) and the line luminosities (from Table 1 of Cañameras et al. 2018). All 7/11 and 8/11 galaxies with [C I](${}^3P_1 - {}^3P_0$) and [C I](${}^3P_2 - {}^3P_1$) coverage, respectively, are securely detected (Nesvadba et al. 2018). Four out of 11 sources have both transitions available. Our SED modeling confirms the lesser AGN contribution to the total L_{IR} reported in Cañameras et al. (2015) ($\max(f_{\text{AGN}}) \sim 30\%$ for 3/11 galaxies, negligible for the rest of the sample).

- **Dannerbauer et al. (2019):** Dubbed the ‘‘Cosmic Eyebrow’’ in analogy with the prototypical strongly lensed SMG ‘‘Cosmic Eyelash’’ (Ivison et al. 2010; Danielson et al. 2011), this source has been selected by cross-matching the *AllWISE* and the *Planck* full-sky compact source catalogs (Díaz-Sánchez et al. 2017). The red *WISE* colors and ultrabright emission detected by *Planck* and SCUBA2 (Jones 2015) have been recently confirmed to arise from two lensed galaxies at $z = 2.04$ by Dannerbauer et al. (2019), who report [C I](${}^3P_1 - {}^3P_0$), CO (4 - 3), CO (3 - 2), and CO (1 - 0) fluxes measured with NOEMA, IRAM/EMIR and GBT, respectively. The NOEMA observations spatially resolve the CO (3 - 2) emission from the A and B components and allow for the deblending of the far-IR emission, assuming an average observed (i.e., magnified) luminosity ratio of $2.8\times$ between the two galaxies. We have assumed this value in order to split the global properties that we derived from the SED modeling (e.g., $L_{\text{IR,tot}} = \mu_{\text{A}}L_{\text{A}} + \mu_{\text{B}}L_{\text{B}} = (1 + 1/2.8)\mu_{\text{A}}L_{\text{A}}$, with $\mu_{\text{A}} = 11 \pm 2$ and $\mu_{\text{B}} = 15 \pm 3$). Here we consider only the component A, to which the [C I](${}^3P_1 - {}^3P_0$) and CO (4 - 3) line emissions are associated.

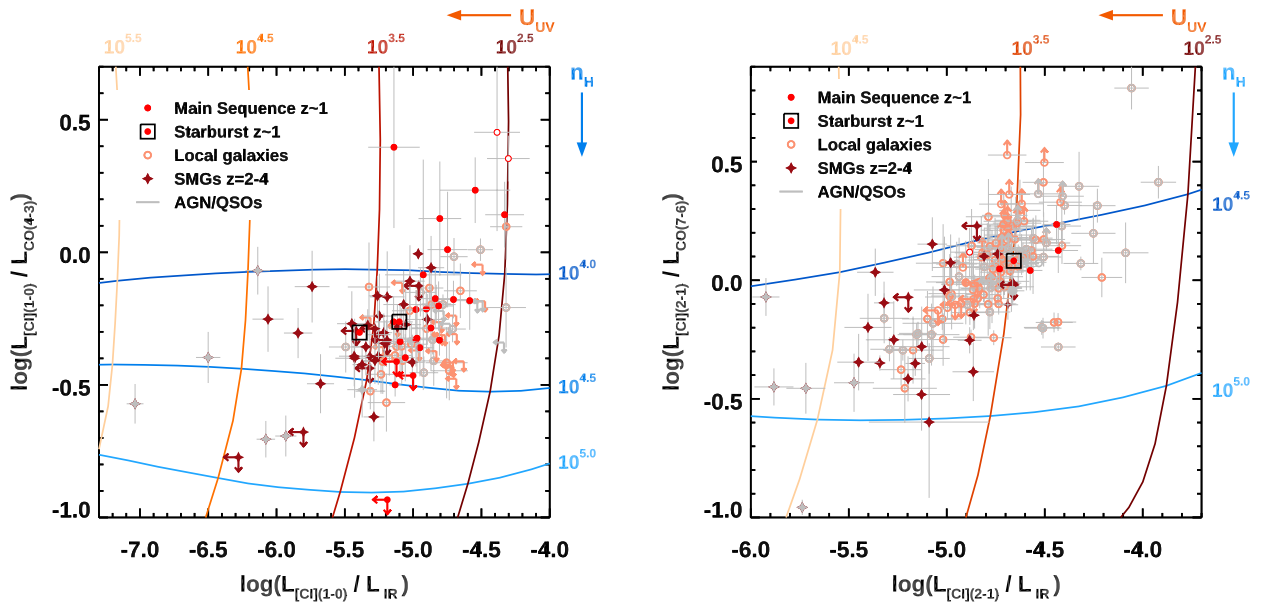


Figure 1. [C I], CO, and L_{IR} planes. *Left:* $L_{[\text{C I}]^3P_1 - ^3P_0} / L_{\text{IR}} - L_{[\text{C I}]^3P_1 - ^3P_0} / L_{\text{CO}(4-3)}$. *Right:* $L_{[\text{C I}]^3P_2 - ^3P_1} / L_{\text{IR}} - L_{[\text{C I}]^3P_2 - ^3P_1} / L_{\text{CO}(7-6)}$. The luminosities are in L_{\odot} . Red solid circles: main sequence galaxies at $z \sim 1$ (this work, V18, Bourne et al. 2019; red empty circles: sources with caveats from the latter) and $z = 2.225$ (Popping et al. 2017); empty black squares: starbursts at $z \sim 1.2$ (V18); empty orange circles: local FTS sample of star-forming galaxies (Liu et al. 2015; Kamenetzky et al. 2016); empty gray circles: local FTS sample with AGN signatures (Liu et al. 2015; Kamenetzky et al. 2016; Véron-Cetty & Véron 2010); dark red solid stars: $z \sim 2-4$ SMGs (Walter et al. 2011; Alaghband-Zadeh et al. 2013; Bothwell et al. 2019; Yang et al. 2017; Andreani et al. 2018; Cañameras et al. 2018; Nesvadba et al. 2018; Dannerbauer et al. 2019; Jin et al. 2019). Gray symbols indicate QSO/AGN-contaminated galaxies. Arrows mark 3σ limits. When not available, we derived CO (4-3) from CO (5-4) or CO (3-2) by applying average corrections for each individual sample (Section 3.1). The blue and red solid lines indicate the tracks of constant density n [cm^{-3}] and intensity of the UV radiation field U_{UV} [Habing units, G_0] from the PDR models by Kaufman et al. (1999).

- **Yang et al. (2017); Andreani et al. (2018):** These authors report $[\text{C I}]^3P_2 - ^3P_1$ measurements for 11 galaxies drawn from a subsample of SMGs from the *Herschel*-Astrophysical Terahertz Large Area Survey (*H-ATLAS*; Eales et al. 2010). The sources have been selected based on their bright *Herschel*/SPIRE 500 μm fluxes ($S_{500} > 100$ mJy), a suitable threshold to identify strongly lensed dusty systems (e.g., Negrello et al. 2010). The redshift confirmation at $z = 2-3.5$ mainly came from CO (1-0) (Harris et al. 2012), followed by NOEMA, ALMA, and APEX/SEPIA 5 campaigns detecting several sub-mm transitions, including both molecular and atomic species (CO, H_2O , and $[\text{C I}]^3P_2 - ^3P_1$) Yang et al. 2017; Andreani et al. 2018). For our analysis, when available we adopted the photometry in Zhang et al. (2018) and the magnification factors mainly derived from 880 μm observations (Bussmann et al. 2013). When not available, we used the photometry in Yang et al. (2017). In total, we retrieve 7 detections at $> 3\sigma$, 2 marginal detections and 2 upper limits on $[\text{C I}]^3P_2 - ^3P_1$. No coverage of the $[\text{C I}]^3P_1 - ^3P_0$ line is available for these sources. All

11 galaxies have at least one detection in CO (4-3), CO (5-4), or CO (7-6).

- **Jin et al. (2019):** We include the SMG at $z = 3.623$ (ID:85001674) with $[\text{C I}]^3P_1 - ^3P_0$ and CO (4-3) detections in ALMA Band 3 (Project ID: 2017.1.00373.S, PI: S. Jin). This and a handful of other sources were selected as residuals in the COSMOS/SCUBA2 850 μm map, after the subtraction of known bright sources (Geach et al. 2017). Here we adopted their “intrinsic” quantities obtained including the effect of the CMB. Notice that the authors rely on a MBB law, since the CMB effect cannot currently be included in Draine & Li (2007) models. However, the final quantities have been corrected to total values to match the same conventions we adopt here. The results do not change using the “observed” values (see Table 3 in Jin et al. 2019).

3. ANALYSIS AND RESULTS

3.1. [C I] and mid-/high- J CO line ratios

In V18 we showed that the $[\text{C I}]^3P_1 - ^3P_0$ /low- J CO luminosity ratio ($J_{\text{upper}} = 1-2$) is constant

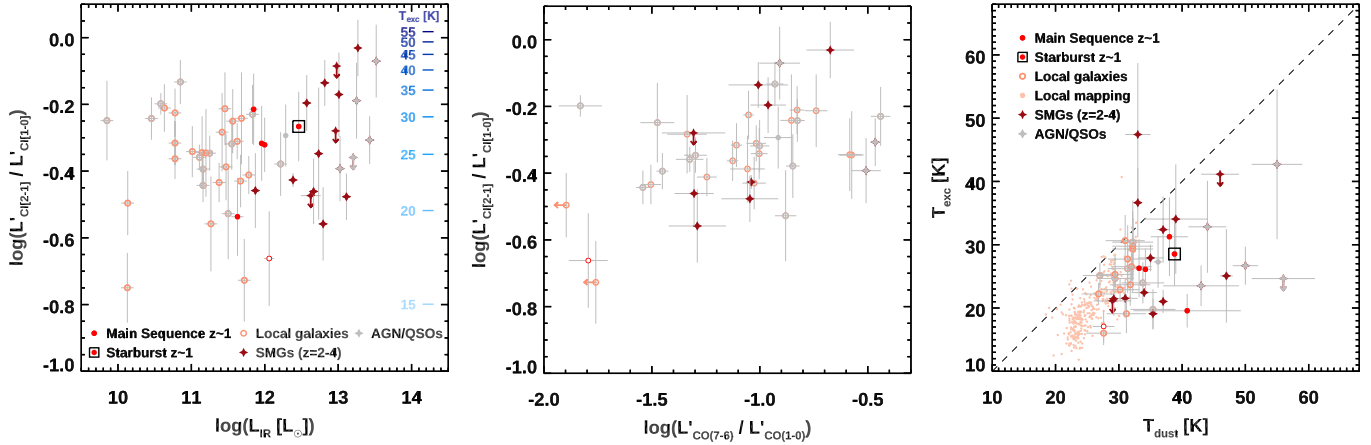


Figure 2. $[C I]^{(3P_2 - 3P_1)} / [C I]^{(3P_1 - 3P_0)}$ line ratio in galaxies. *Left:* $L'_{[C I]^{3P_2-3P_1}} / L'_{[C I]^{3P_1-3P_0}}$ ratio as a function of the total L_{IR} . Symbols and colors indicate galaxies as in Figure 1, when both $[C I]^{(3P_1 - 3P_0)}$ and $[C I]^{(3P_2 - 3P_1)}$ detections are available. The blue ticks show the excitation temperature T_{exc} corresponding to the $L'_{[C I]^{3P_2-3P_1}} / L'_{[C I]^{3P_1-3P_0}}$ ratio on the Y-axis, assuming a local thermal equilibrium and optically thin [C I] lines. *Center:* [C I] line ratio as a function of $L'_{CO(7-6)} / L'_{CO(4-3)}$. *Right:* the excitation temperature T_{exc} as a function of the dust temperature from SED fitting with a single-component, optically thin modified black body model. The filled small orange circles show the resolved mapping from Jiao et al. (2019b), with T_{dust} from *Herschel* colors. The dashed black line shows the one-to-one relation. For clarity, we do not show the lower limits on the [C I] line ratios and on T_{exc} for the local sample.

over $z = 0 - 4$ and irrespectively of the galaxy type, suggesting that [C I] and CO are well correlated on global scales. This extended previous findings for local nuclear starbursts (e.g., Gerin & Phillips 2000; Jiao et al. 2017, now confirmed on sub-galactic scales, Jiao et al. 2019a) and high-redshift SMGs (Yang et al. 2017) to the bulk of main sequence galaxies. Here we focus on the comparison between [C I] and mid-/high- J CO emission ($J_{upper} = 3 - 7$), the latter expected to arise from warmer and denser molecular phases. Figure 1 shows $L_{[C I]^{3P_1-3P_0}} / L_{CO(4-3)}$ as a function of $L_{[C I]^{3P_1-3P_0}} / L_{IR}$ and $L_{[C I]^{3P_2-3P_1}} / L_{CO(7-6)}$ against $L_{[C I]^{3P_2-3P_1}} / L_{IR}$. The luminosities are all expressed in L_{\odot} . The choice of these line ratios is dictated by the close rest-frame frequencies of these [C I]-CO couples, which make them often observed simultaneously. The use of line ratios mitigate the consequences of lensing, but a differential effect can still affect the emission arising from distinct ISM phases. We refer the reader to the original works for a detailed description of differential lensing on high-redshift sub-mm galaxies. On the contrary, this is not a concern for local and main sequence galaxies. Since some galaxies do not have direct observations of the CO (4-3) line available, but were observed in an adjacent transition, we used the following line ratios to correct to CO (4-3): $L_{CO(3-2)} / L_{CO(4-3)} = 0.57$ and $L_{CO(5-4)} / L_{CO(4-3)} = 1.36$ for a total of 9 high-redshift SMGs and $L_{CO(5-4)} / L_{CO(4-3)} = 0.92$ for 5 main sequence galaxies. These factors are the observed average values for galaxies in each sample with both CO lines

available. The results do not change adopting median corrections. The slight difference in $L_{CO(5-4)} / L_{CO(4-3)}$ for SMGs and main sequence galaxies might suggest a different slope of the CO SLED (e.g., Daddi et al. 2015), but it is not significant at this stage. No correction was applied to $L_{[C I]^{3P_2-3P_1}} / L_{CO(7-6)}$.

In both panels we find a gradient of observables across the populations. High-redshift SMGs appear to have lower $L_{[C I]^{3P_1-3P_0}} / L_{CO(4-3)}$ and $L_{[C I]^{3P_2-3P_1}} / L_{CO(7-6)}$ ratios than the main sequence and local LIRGs. A similar trend is appreciable for $L_{[C I]^{3P_1-3P_0}} / L_{IR}$ and $L_{[C I]^{3P_2-3P_1}} / L_{IR}$, as commented in V18. We quantify the differences in the luminosity ratio parent distributions by running the set of non-parametric two-sample tests from the *twosamp* task in the IRAF/STSDAS package (Feigelson & Nelson 1985), including the censored data, generally in the form of upper limits on the [C I] luminosities. A notable exception is a substantial number of lower limits (21 galaxies) on the $L_{[C I]^{3P_2-3P_1}} / L_{CO(7-6)}$ ratios for the sample of local LIRGs without AGN signatures. Since doubly censored data are not allowed by the two sample tests, we separately ran the latter on the population of lower and upper limits. This suite of tests includes the logrank, the Gehan, Peto & Peto, and Peto & Prentice Generalized Wilcoxon tests. Moreover, Table 4 reports the mean and its uncertainties for each sample using the Kaplan & Meier (1958) estimator. We exclude galaxies with a substantial contribution to the IR emission and,

potentially, to the line excitation from AGN/QSOs, since we cannot securely disentangle the contribution to the dust emission heated by star formation from the SED modeling. We show the position of such galaxies in the plots, but their properties are driven by the large L_{IR} ensuing the emission from dusty tori in the mid-IR (V18).

The probability that the observed distributions of $L_{[\text{C I}]^3 P_1 - ^3 P_0} / L_{\text{IR}}$ ratios are drawn from the same parent distributions is $p < 0.0001$ for all the tests when comparing the high-redshift SMGs and the main sequence galaxies at $z \sim 1$. Similarly we retrieve $p < 0.006$ when considering the SMGs and the local galaxies, with the exception of the Peto & Prentice generalized Wilcoxon test returning a p -value of $p = 0.044$. We obtain marginally consistent distributions when comparing local and main sequence galaxies at $z \sim 1$ ($p = 0.006 - 0.016$). Turning to $L_{[\text{C I}]^3 P_1 - ^3 P_0} / L_{\text{CO}(4-3)}$, we find evidence for different parent distributions when comparing local and main sequence galaxies ($p < 0.004$), but not for main sequence objects and SMGs ($p = 0.062 - 0.56$), nor local galaxies and SMGs ($p = 0.033 - 0.089$, except for the Peto & Prentice test returning $p = 0.001$). For what concerns the distributions of the $L_{[\text{C I}]^3 P_2 - ^3 P_1} / L_{\text{IR}}$ ratios, we find $p < 0.001$ for all the tests when comparing the high-redshift SMGs and the local galaxies. Similarly, we find $p < 0.002$ when comparing main sequence objects at $z \sim 1$ and SMGs, with the exception of the Peto & Prentice test ($p = 0.014$). On the contrary, the local and main sequence galaxies are consistent with being drawn from the same parent distributions ($p = 0.03 - 0.49$), the p -values spanning a different range when considering separately upper and lower limits in the local sample, but still safely larger than meaningful thresholds to reject the null hypothesis. An identical conclusion is reached when comparing the $L_{[\text{C I}]^3 P_2 - ^3 P_1} / L_{\text{CO}(7-6)}$ ratios ($p = 0.02 - 0.76$ when comparing local and main sequence galaxies at $z \sim 1$; $p = 0.0 - 0.021$ for main sequence and high-redshift SMGs; $p < 0.002$ for local galaxies and SMGs). We stress that only a handful of main sequence galaxies with $[\text{C I}](^3 P_2 - ^3 P_1)$ and $\text{CO}(7-6)$ measurements are currently available and, thus, these results will have to be validated with larger samples.

The results of the tests on the $[\text{C I}]/\text{IR}$ luminosity ratios confirm what we found in the less numerous sample of V18: the local starbursts and $z \sim 1$ main sequence galaxies share similar properties, while significantly differing from the high-redshift

SMGs. Here we reach similar conclusions also for the $L_{[\text{C I}]^3 P_2 - ^3 P_1} / L_{\text{CO}(7-6)}$ ratios, pointing towards an intrinsic difference of the physical properties of the dense and diffuse gas in these populations. The conclusions based on $L_{[\text{C I}]^3 P_1 - ^3 P_0} / L_{\text{CO}(4-3)}$ are less clear: our samples appear more homogeneous, as noted for $[\text{C I}](^3 P_1 - ^3 P_0) / \text{CO}(2-1)$ in V18. This might be due to the CO SLEDs of the different samples being more similar at low and mid- J transitions, while clearly diverging at higher J_{upper} , where the distributions keep rising for strongly starbursting systems, while declining for “normal” disks (e.g., Liu et al. 2015; Daddi et al. 2015; Yang et al. 2017; Cañameras et al. 2018).

Since $[\text{C I}]$, mid-/high- J CO, and L_{IR} trace the low density, high density gas, and the SFR, respectively, we interpret these trends as evidence for increased dense molecular gas fractions and higher star formation efficiencies ($\text{SFE} = \text{SFR}/M_{\star}$) in high-redshift SMGs than main sequence galaxies and local LIRGs. Assuming that the SMG population is dominated by starbursting galaxies (i.e., several times above the main sequence at their redshifts), this is consistent with the picture derived from classical CO-based studies (e.g., Solomon et al. 1997; Gao & Solomon 1999, 2004; Daddi et al. 2010; Genzel et al. 2015; Yamashita et al. 2017; Tacconi et al. 2018) and dense molecular gas tracers (e.g., HCN, Gao et al. 2007). CO(7-6) is arguably a better tracer of the dense molecular gas than mid- J ($J_{\text{upper}} = 3 - 5$) and, thus, the separation of the various populations in the right panel of Figure 1 is more evident (despite the general caveat of possible contributions of XDR, Meijerink et al. 2007, or shocks, Lee et al. 2019, to the high- J CO emission). Alternatively, these panels might be understood as manifestations of the (integrated) Schmidt-Kennicutt relation (Schmidt 1959; Kennicutt 1998a). Again, the better separation of the various populations in the right panel of Figure 1 derives from the tighter correlation with L_{IR} of CO(7-6) than CO(4-3) (Greve et al. 2014; Liu et al. 2015; Kamenetzky et al. 2016; Lu et al. 2015, 2017). CO(7-6) shows in fact the tightest correlation with L_{IR} among the CO transitions, at least in the local universe (e.g., Lu et al. 2015; Liu et al. 2015).

3.2. $[\text{C I}]$ line ratios and gas temperature

Given its simple three-level structure, the $[\text{C I}](^3 P_2 - ^3 P_1) / [\text{C I}](^3 P_1 - ^3 P_0)$ line ratio can serve as a measurement of the gas kinetic temperature (see Papadopoulos et al. 2004 for a full derivation). Under the assumption of local thermal equilibrium, the kinetic temperature equals the excitation tem-

Table 4. Mean line luminosity ratios.

	$\log(L_{[\text{C I}]^3 P_1 - ^3 P_0}/L_{\text{IR}})$	$\log(L_{[\text{C I}]^3 P_1 - ^3 P_0}/L_{\text{CO}(4-3)})$	Detections/Censored
Local galaxies	-5.075 ± 0.043	-0.390 ± 0.027	19/18
Main sequence $z \sim 1$	$-4.908 \pm 0.044^\dagger$	$-0.243 \pm 0.064^\dagger$	21/3
SMGs $z \sim 2 - 4$	$-5.336 \pm 0.060^\dagger$	$-0.348 \pm 0.032^\dagger$	29/7
	$\log(L_{[\text{C I}]^3 P_2 - ^3 P_1}/L_{\text{IR}})$	$\log(L_{[\text{C I}]^3 P_2 - ^3 P_1}/L_{\text{CO}(7-6)})$	
Local galaxies (upper)	-4.792 ± 0.025	-0.011 ± 0.020	62/5
Local galaxies (lower)	-4.707 ± 0.025	$0.108 \pm 0.027^\dagger$	62/21
Main sequence $z \sim 1$	-4.612 ± 0.078	0.114 ± 0.031	5/0
SMGs $z \sim 2 - 4$	-5.084 ± 0.050	-0.193 ± 0.044	21/3
	$L'_{[\text{C I}]^3 P_2 - ^3 P_1}/L'_{[\text{C I}]^3 P_1 - ^3 P_0}$		
Local galaxies	0.437 ± 0.028		20/0
Main sequence $z \sim 1$	0.465 ± 0.057		4/0
SMGs $z \sim 2 - 4$	0.476 ± 0.057		10/3

NOTE— † : The mean value is formally biased, since the lowest value is an upper limit.

perature $T_{\text{exc}}/\text{K} = 38.8/\ln(2.11/R)$, where $R = L'_{[\text{C I}]^3 P_2 - ^3 P_1}/L'_{[\text{C I}]^3 P_1 - ^3 P_0}$, which further requires the lines to be optically thin (Schneider et al. 2003; Weiß et al. 2003; Walter et al. 2011).

We show in Figure 2 the available galaxies with both [C I] lines. The observed $L'_{[\text{C I}]^3 P_2 - ^3 P_1}/L'_{[\text{C I}]^3 P_1 - ^3 P_0}$ ratios of the local, main sequence at $z \sim 1$ and high-redshift SMG samples are fully consistent (Table 4) and we do not find any significant correlation with L_{IR} . Notice that we considered only the detections of both [C I] lines for the local sample, since the large number of upper limits on $[\text{C I}](^3 P_1 - ^3 P_0)$ does not affect the mean value reported here. We further excluded # 35349 from the sample of main sequence galaxies, given the mismatch of the two [C I] line profiles. Converting the line ratios into temperatures, we find a mean temperature of $\langle T_{\text{exc}} \rangle = 25.6 \pm 1.0$ K for the whole compilation, including upper limits. Nevertheless, the scatter of the measurements is substantial: we find an interquartile range of $\Delta T_{\text{exc}} = 8.0$ K centered on a median value of $T_{\text{exc}} = 25.1$ K. These values are consistent with our estimates in V18 and with previous measurements reported for individual subsamples ($\langle T_{\text{exc}} \rangle = 29.1 \pm 6.3$ K, Walter et al. 2011; $T_{\text{exc}} = 21 - 57$ K, Nesvadba et al. 2018). Note that we excluded the objects contaminated by AGN/QSOs from this calculation. The mean temperature value is slightly lower than the commonly adopted $T_{\text{exc}} = 30$ K (e.g., Alaghband-Zadeh et al. 2013; Both-

well et al. 2017). While this has a minor impact on the calculation of [C I] masses from $[\text{C I}](^3 P_1 - ^3 P_0)$, lower temperatures affect such estimates using $[\text{C I}](^3 P_2 - ^3 P_1)$ as a tracer (e.g., Figure 2 in Weiß et al. 2005).

We further compared the excitation temperature T_{exc} ($\propto L'_{[\text{C I}]^3 P_2 - ^3 P_1}/L'_{[\text{C I}]^3 P_1 - ^3 P_0}$) with the luminosity-weighted dust temperature T_{dust} from the modeling of the SED with a single-component, optically thin modified black body curve (Figure 2). We chose this simple parametrization to facilitate the comparison with literature data. However, similar conclusions can be drawn when comparing T_{exc} with the mean intensity of the radiation field $\langle U \rangle$ from the multi-component Draine & Li (2007) models, an alternative tracer of the dust heating correlated with a mass-weighted T_{dust} ($\langle U \rangle = (T_{\text{dust}}[\text{K}]/18.9)^{6.04}$, Magdis et al. 2017; Schreiber et al. 2018). The dust temperature is frequently assumed as a proxy for T_{exc} and the gas temperature, absent a direct estimate, and $T_{\text{dust}} = T_{\text{kin}} = T_{\text{exc}}$ under perfect LTE, owing to the efficient dust and gas coupling (Carilli & Walter 2013; da Cunha et al. 2013). Here we identify a mild correlation between T_{exc} and T_{dust} only for the galaxy-integrated emission from local objects with secure [C I] line detections ($\rho = 0.47, 0.62$, and 0.63 Kendall, Spearman, and Pearson’s correlation coefficients, respectively), in agreement with previous results, holding down to sub-galactic scales (Jiao et al. 2017, 2019a). However, applying a generalized Kendall’s

tau correlation coefficient to include the lower limits on T_{exc} with the task *bhkmeth* in IRAF (Feigelson & Nelson 1985), we find significant probabilities that T_{exc} and T_{dust} are not correlated ($p = 0.3071$). Similarly, at this stage there are no hints of a strong correlation between T_{exc} and T_{dust} for the high-redshift galaxies taken alone, nor for the compilation as a whole, with similar probabilities from the generalized Kendall’s tau test or even considering detections only. However, as clear from Figure 2, this result might stem from the relatively sparse high-redshift sample and its low number statistics. Notice that in the vast majority of the cases, we find $T_{\text{exc}} < T_{\text{dust}}$.

On the contrary, a mild correlation is present when comparing $L'_{\text{CO}(7-6)}/L'_{\text{CO}(1-0)}$ and $L'_{[\text{C I}]^3 P_2 - ^3 P_1}/L'_{[\text{C I}]^3 P_1 - ^3 P_0}$ ($p = 0.0089$ probability that the two ratios do not correlate from the generalized Kendall’s tau test; $\rho = 0.39, 0.52, \text{ and } 0.57$ Kendall, Pearson, and Spearman’s correlation coefficients, respectively, considering only the detections, Figure 2). When not directly measured, for a handful of SMGs we estimated $L'_{\text{CO}(1-0)}$ by converting $L'_{\text{CO}(3-2)}$ luminosities following Bothwell et al. (2013). No usable low- J CO transitions are available for our sample of main sequence galaxies at $z \sim 1$ with coverage of both [C I] lines, excluded the aforementioned #35349. The observed correlation suggests that the CO and [C I] excitation conditions are related and, by extension, that the temperature traced by [C I] increases for steeper CO SLEDs.

4. DISCUSSION

4.1. A view on the ISM: modeling of the photodissociation regions

We now attempt to provide further insight into the physical conditions of the ISM in galaxies by modeling the [C I], CO, and IR emission following the classical recipes for photodissociation regions (PDRs). Here we adopt the one-dimensional models by Kaufman et al. (1999) in the updated version released with the PHOTODISSOCIATION REGION TOOLBOX³ (PDRT; Kaufman et al. 2006; Pound & Wolfire 2008). The models solve simultaneously for the chemistry, thermal balance and radiative transfer, assuming metal, dust, and polycyclic aromatic hydrocarbons (PAHs) abundances, and a gas microturbulent velocity dispersion. For each combination of properties, a model is described in terms of the (number) density of H nuclei $n [\text{cm}^{-3}]$ and the in-

tensity of the incident far-ultraviolet radiation (FUV, $6 \text{ eV} < h\nu < 13.6 \text{ eV}$) G_0 in units of the local Galactic interstellar field ($G_0 = 1.6 \times 10^{-3} \text{ erg cm}^{-2} \text{ s}^{-1}$, Habing 1968). The original models cover the $10 \leq n \leq 10^7 \text{ cm}^{-3}$ and $10^{-0.5} \leq G_0 \leq 10^{6.5}$ ranges in step of 0.25 dex. However, we rebinned the templates to a $5 \times$ finer grid before fitting the data: this did not affect the final best-fit estimate of the density and intensity of the radiation field, but it allowed us to assess the statistical uncertainties of the fit. We computed the latter by applying the χ^2 criterion by Avni (1976), fixing $\Delta\chi^2 < 2.71$ corresponding to a 90% confidence interval. We also adopted a purely numerical approach by bootstrapping 1000 times the observed flux ratios within their errors and using the 68%, 90%, and 95% inter-percentile ranges as the corresponding confidence intervals. The best-fit model results from the χ^2 minimization of the line and continuum emission ratios.

To the standard ratios available from PDRT, we added the [C I]/IR ratios. The latter mainly depend on G_0 through the IR emission due to the dust clouds absorbing the UV incident emission and reprocessing it at longer wavelength. On the other hand, in standard one-dimensional PDR models, [C I] arises from the $\text{C}^+/\text{C}/\text{CO}$ transition layer, which can be pushed deeper into the cloud when the FUV field increases, but remaining substantially unchanged, so that the column density of C does not depend on G_0 (e.g. Tielens & Hollenbach 1985; Kaufman et al. 1999; Gerin & Phillips 2000). We computed the IR intensity map as $2 \times 1.3 \times 10^{-4} G_0 \text{ erg cm}^{-2} \text{ s}^{-1} \text{ sr}^{-1}$, including the contribution to the global dust heating from photons outside the FUV regime and considering the finite slab geometry (Kaufman et al. 1999). An extra factor of $2 \times$ should be included when considering the case of multiple clouds filling the beam – as for our unresolved measurements –, being illuminated from every side. In this case, the optically thin IR emission from both the near and far side of clouds would be visible (Kaufman et al. 1999). However, a similar factor applies to the optically thin [C I] emission, canceling out this effect. We adopted the total IR luminosity $L_{\text{IR}}(8-1000 \mu\text{m})$ due to star-formation (i.e., removing the AGN contribution) from the SED modeling as the estimate for IR. The only exceptions are high-redshift QSOs, where the AGN emission dominates the far-IR SED and we could not distinguish the contribution from star formation. We therefore used the total L_{IR} and we highlighted their location in the relevant plots. As noted above, systematic deviations in the [C I]/IR ratios are largely due to this effect (V18). Notice also that the Draine & Li (2007) suite of templates accounts for the independent contributions to the total emission from

³ <http://dustem.astro.umd.edu/pdrt>

the diffuse ISM and the PDRs, but the available data does not allow us to discriminate between these two components. We therefore used the combined, total IR emission for the modeling.

While G_0 is constrained by [C I]/IR, a [C I]/mid- or high- J_{upper} CO ratio is an effective tracer of the gas density, being almost insensitive to G_0 . Therefore, the combination of [C I]/IR and [C I]/mid- or high- J_{upper} CO allows for a full determination of the PDR properties. This is clear from the nearly perpendicular tracks in Figure 1⁴. Notice that our grid of models is different from the one in Alaghband-Zadeh et al. (2013) due to the diverse approaches to map L_{IR} into G_0 (Figure 8 in Appendix). These models were applied to the available combinations of observed ratios. We show the n, G_0 values from the modeling of $L_{[\text{C I}]^3P_1 - ^3P_0}$, $L_{\text{CO}(4-3)}$, and L_{IR} in Figure 3. The median location of the local LIRGs, main sequence galaxies, and high-redshift SMGs are also shown in comparison with regions occupied by local main sequence galaxies (Malhotra et al. 2001), spirals and giant molecular clouds, starbursts, nuclei and OB regions (Stacey et al. 1991), and ULIRGs (Davies et al. 2003). The conclusions about the observed line ratios are naturally reflected on the similar G_0/n ratios for main sequence galaxies at $z \sim 1$ and local LIRGs, both lower than for SMGs. The trend is driven by the increasing G_0 ($\propto (L_{[\text{C I}]^3P_1 - ^3P_0}/L_{\text{IR}})^{-1}$). The median location and the distribution of the n, G_0 values for main sequence galaxies at $z \sim 1$ is also consistent with the approximate boundaries for local similar samples and spiral and GMCs, areas completely devoided of SMGs.

Therefore, interpreting the gas and dust emission according to photodissociation region modeling further suggests similar ISM conditions in main sequence galaxies and local LIRGs, both less extreme than in high-redshift SMGs.

4.1.1. Caveats and shortcomings of PDR modeling

The modeling presented above allows only for a simple interpretation of basic combinations of line ratios, especially considering the lack of spatial resolution. However, the trends identified in the previous Section should be treated as an order of magnitude indication, since the modeling suffers from multiple limitations, as previously noted by several authors who attempted a similar analysis on part of the samples col-

lected here (Appendix E, Alaghband-Zadeh et al. 2013; Bothwell et al. 2017; Cañameras et al. 2018, and references therein). Here we report further evidence that the view on the ISM offered by simple one-dimensional modeling is likely not sufficient to capture the physical complexity of this medium. As shown in Figure 1, galaxies in the [C I] $(^3P_1 - ^3P_0)$ /CO(4-3)/IR and [C I] $(^3P_2 - ^3P_1)$ /CO(7-6)/IR planes are mapped into different regions of the n, G_0 parameter space, the former line combination returning lower densities and intensities of the FUV radiation fields than the latter. This likely reflects gas in different phases, warmer and denser in the [C I] $(^3P_2 - ^3P_1)$ /CO(7-6)/IR diagram than in [C I] $(^3P_1 - ^3P_0)$ /CO(4-3)/IR. The adopted models struggle to reproduce the densest molecular gas, given the assumption of a moderate constant attenuation $A_V = 1.8$ mag. We quantified the effect of modeling [C I] $(^3P_1 - ^3P_0)$ or [C I] $(^3P_2 - ^3P_1)$ keeping CO+IR fixed for the galaxies with both [C I] lines available. Figure 8 in Appendix shows that using [C I] $(^3P_2 - ^3P_1)$ results in ~ 0.5 and ~ 0.3 dex larger n and G_0 than when adopting [C I] $(^3P_1 - ^3P_0)$ respectively, explaining most of the shift observed in Figure 1. We similarly tested the impact of using [C II] in lieu of L_{IR} for a sub-sample of the SPT-SMGs at $z \sim 4$. Both these quantities are primarily dependent on G_0 , so n is not affected by this choice. Figure 8 shows that, despite the large scatter, modeling [C II] or L_{IR} gives consistent results. These tests show that the larger spread of n, G_0 reported when fitting simultaneously all the available luminosity ratios (Danielson et al. 2011; Alaghband-Zadeh et al. 2013) likely results from the inability of a single PDR model to capture a multi-component ISM.

4.2. Gas and dust temperatures

In Section 3.2 we reported the presence of a mild correlation between the gas excitation temperature T_{exc} derived from the [C I] line ratio and the luminosity-weighted dust temperature T_{dust} (or the mean intensity of the radiation field $\langle U \rangle$, Figure 2) for local galaxies, but also the lack of indications that a similarly significant correlation is in place for the high-redshift objects, possibly because of the sparsity of such sample. We further found that, generally, $T_{\text{exc}} \lesssim T_{\text{dust}}$ in our compilation, with a rather constant T_{exc} across the different populations and redshifts. If confirmed, this can be explained considering that, in first approximation, [C I] arises from a thin transitioning layer between CO and [C II], being insensitive to the ambient UV radiation field. Moreover, the fact that $T_{\text{exc}} \lesssim T_{\text{dust}}$ is consistent with what is reported for a subsample of high-redshift SMGs collected here (Nesvadba et al. 2018). This might

⁴ The intensity ratio maps from the Kaufman et al. (1999) models are available in .fits format in the original PDRT website.

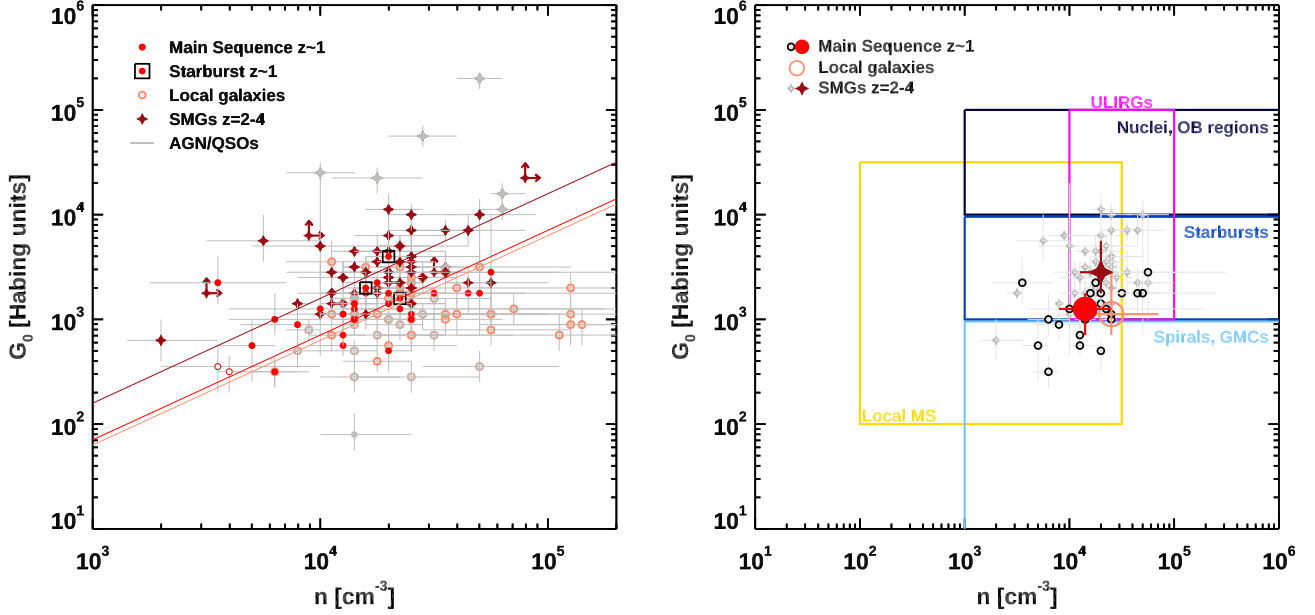


Figure 3. Modeling of the photodissociation regions. *Left:* Best-fit gas density n [cm^{-3}] and intensity of the UV radiation field U_{UV} [Habing units, G_0] from the PDR models by Kaufman et al. (1999) on the observed $[\text{C I}]({}^3P_1 - {}^3P_0)$, $\text{CO}(4-3)$, and the IR estimates. Colors and symbols are as in Figure 1. The dark, red, and light solid lines mark the loci of constant G_0/n equal to the medians of the SMG, main sequence, and local galaxies, respectively. *Right:* Median locations of the main sequence galaxies (red solid circle), local starbursts sample (open orange circle), and SMGs at $z \sim 2-4$ (dark red solid star) in the same plane as in the left panel. The error bars on the median represent the 16% - 84% inter-percentile range. For reference, we show the location of the individual main sequence galaxies (black open circles) and the SMGs (gray stars). The blue solid contours enclose the regions occupied by local galactic nuclei/OB regions, Starbursts, and Spirals/GMCs from Stacey et al. (1991). The yellow square indicate the position of local main sequence galaxies from Malhotra et al. (2001). The purple box shows the location of ULIRGs from Davies et al. (2003).

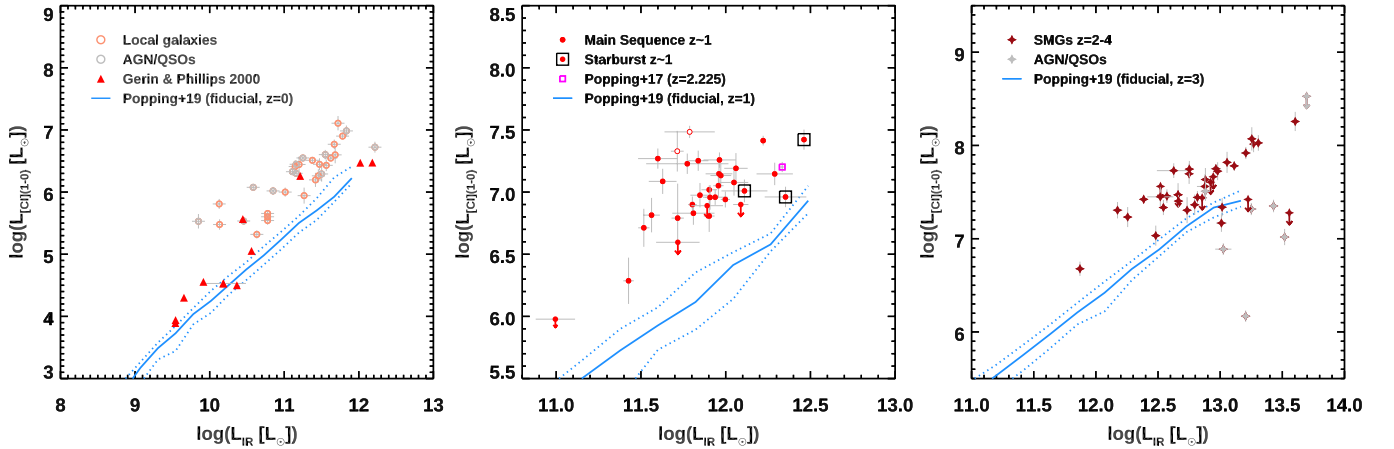


Figure 4. Semi-analytical modeling of $[\text{C I}]({}^3P_1 - {}^3P_0)$ emission in galaxies. *Left:* Empty orange and gray circles mark the local sample of starburst galaxies without and with AGN signatures. The red filled triangles show the galaxies from Gerin & Phillips (2000). *Center:* The red filled circles show the main sequence galaxies at $z \sim 1$ (red empty circles: sources with caveats from Bourne et al. 2019). The empty black squares indicate the starbursts at $z \sim 1.2$. To highlight the different redshift, the empty purple square marks the main sequence object at $z = 2.225$ from Popping et al. (2017). *Right:* The dark red solid stars show $z \sim 2-4$ SMGs. The gray solid stars indicate QSO/AGN-dominated galaxies. Arrows mark 3σ upper limits on $[\text{C I}]$. In every panel, the blue solid and dotted lines indicate the fiducial model by Popping et al. (2019a) and its 16% and 84% percentiles at the average redshift of the samples.

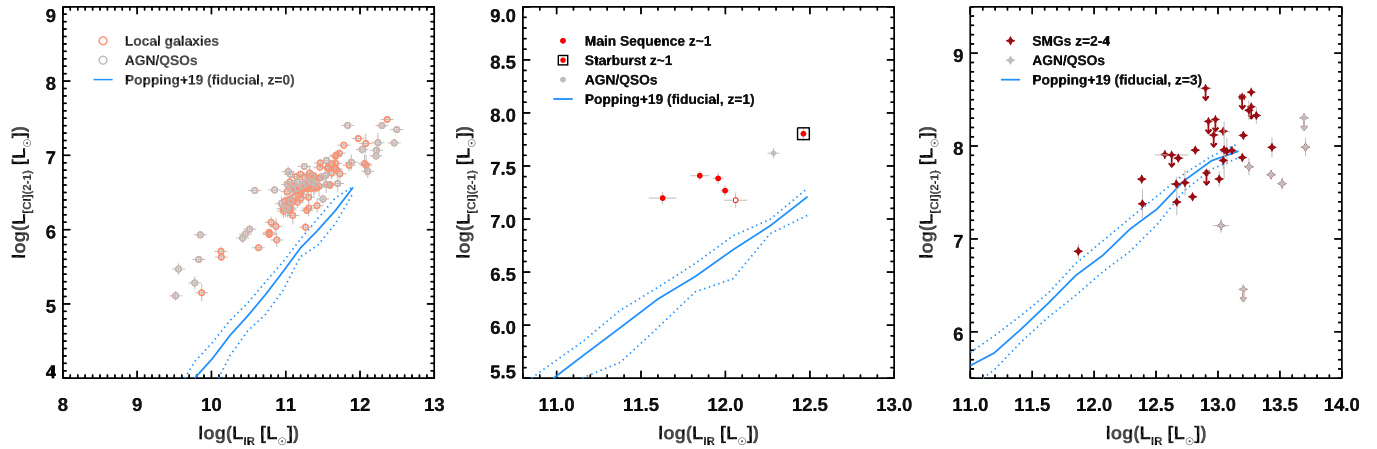


Figure 5. Semi-analytical modeling of [C I] ($^3P_2 - ^3P_1$) emission in galaxies. Symbols and colors indicate galaxies as in Figure 4, when a [C I] ($^3P_2 - ^3P_1$) estimate is available. We did not include any upper limits for the local sample in order to avoid crowding the panel.

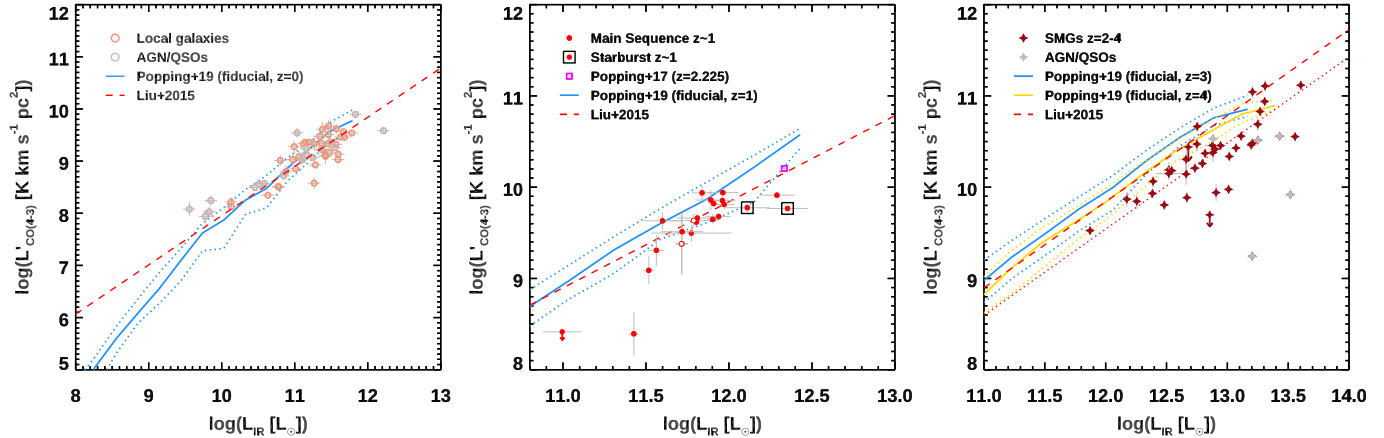


Figure 6. Semi-analytical modeling of CO (4 – 3) emission in galaxies. Symbols and colors indicate galaxies as in Figure 4, when a CO (4 – 3) detection is available (no correction from other CO transition is shown here). In every panel, the dashed red lines indicate the $L_{\text{IR}}-L'_{\text{CO}(4-3)}$ correlation from Liu et al. (2015). In the right panel, the blue and gold lines indicate the fiducial models from Popping et al. (2019a) and their 16% and 84% percentiles at $z = 3$ and $z = 4$, respectively. The red dotted line indicates the Liu et al. (2015) correlation scaled by -0.3 dex as reported in the original paper for starbursts/SMGs.

suggest that gas and dust are not in thermal equilibrium (Cañameras et al. 2015; Nesvadba et al. 2018). Alternatively, considering a more realistic multi-phase ISM, T_{dust} might be determined by a hot component dominating the far-IR emission close to the peak and physically closer to the starbursting regions, while [C I] and the cold dust extend further out, tracing the bulk of the mass of the molecular gas (V18, Nesvadba et al. 2018). Our findings agree with recent findings by Jiao et al. (2019a), who retrieve a moderate $T_{\text{exc}}-T_{\text{dust}}$ correlation in resolved maps of local galaxies (Section 3.2). We do find $T_{\text{exc}} \lesssim T_{\text{dust}}$ for the high-redshift sample as for the local resolved objects (Jiao et al. 2019b) and compatibly with the results by Bothwell et al. (2017) based on a line modeling approach. Here we note that, while T_{exc} is derived in a consistent way across different papers, T_{dust} is highly susceptible of strong variations due to the available photometry and the adopted parametrization of the IR SED. In particular, the lack of coverage of the peak of the emission strongly affects the T_{dust} estimate while classical single-temperature modified black body curves cannot reproduce the observed mid-IR emission, suggesting the existence of multi-component dust along with the ISM (Draine & Li 2007; Galliano et al. 2011; Magdis et al. 2012b; Casey et al. 2014; Schreiber et al. 2018; Liang et al. 2019). Jiao et al. (2019a) estimate T_{dust} by assuming a gray body with $\beta = 2$ modeling the rest-frame 70/160 μm ratio, a color that we cannot directly measure at high redshift. On the other hand, we fit the whole available far-IR SED with a single-temperature MBB leaving β free to vary and assuming an optically thin emission, a common choice allowing for a direct comparison with data in the literature. This latter condition might have to be reconsidered, especially for strongly starbursting objects and SMGs. As shown by Cortzen et al. (submitted), removing this constraint in the SED modeling allows them to derive $T_{\text{dust}} = 52 \pm 5$ K for GN20, the strongest outlier in Figure 2. This is more consistent with $T_{\text{exc}} = 48_{-9}^{+15}$ K from [C I] than in the optically thin case shown in Figure 2 ($T_{\text{dust}} = 33 \pm 2$ K). At the current stage, when removing the $T_{\text{exc}} \gg T_{\text{dust}}$ outliers, the correlation between these two quantities in the high-redshift sample remains weak. The possible future extension of the results on the optical depth of GN20 to the general population of strongly starbursting systems at high redshift (including the role of the cosmic microwave background da Cunha et al. 2013; Zhang et al. 2016), might change this conclusion (e.g., Jin et al. 2019). Finally, we note that we consistently modeled the dust emission for all galaxies at different redshifts. If a significant evolution with time were present, e.g., due to a metallicity change, this could

affect the current results. However, given the large stellar masses and SFRs of the objects collected in this work, metallicity is unlikely to play a major role.

4.3. Neutral atomic carbon in a cosmological galaxy evolution context

The access to a large statistical sample of galaxies covering wide ranges of redshifts and physical conditions allows us to start exploring the role played by neutral atomic carbon in a broader cosmological context of galaxy evolution, an operation so far accessible for a few CO transitions, dust, and increasingly for the bright [C II] emission thanks to similarly numerous samples coming online (e.g., Carilli & Walter 2013; Tacconi et al. 2018; Zanella et al. 2018; Liu et al. 2019, to mention a few recent efforts). Here we compared the [C I] and CO line luminosities from our compilation with the semi-analytical model from Popping et al. (2019a). Briefly, the authors adopted the latest version of the ‘Santa Cruz’ galaxy formation model (Somerville & Primack 1999; Somerville et al. 2001; Popping et al. 2014; Somerville et al. 2015) as the input to shape the emission of sub-mm CO, [C II], and [C I] lines (Krumholz 2014; Narayanan & Krumholz 2017). They applied various subgrid recipes to describe the dense and diffuse gas distribution, the density profile within molecular clouds, the clumping of the medium, the UV and cosmic ray fluxes regulating the ionization and chemistry of the clouds. By combining chemical equilibrium networks and radiative transfer models with sub-grid models, Popping et al. (2019a) finally obtained different sets of CO, [C II], and [C I] luminosities emerging from galaxies and readily comparable with observations. We refer the reader to the original paper for further details.

Figures 4, 5, and 6 show the [C I](${}^3P_1 - {}^3P_0$) [C I](${}^3P_2 - {}^3P_1$) and CO(4 – 3) luminosities of our samples of galaxies compared with the predictions from the fiducial model by Popping et al. (2019a). We show the samples divided in redshifts bins and galaxy type (local LIRGs, main sequence galaxies at $z \sim 1$, and SMGs at $z = 2 - 4$, Section 2). As in previous plots, we also show the position of galaxies with contamination from AGN/QSOs. For reference, in Figure 4 we display the local galaxies from Gerin & Phillips (2000) originally reported in Popping et al. (2019a). We further remind the reader that we corrected both the measurements of the dust and line emission of the local galaxies for the aperture correction (V18, Liu et al. 2015). Such correction is identical for L_{IR} and the line luminosity, therefore moving the galaxies diagonally in the panels. Moreover, we converted the tracks originally

expressed as a function of SFR into L_{IR} by applying the Kennicutt (1998b) conversion for a Chabrier (2003) initial mass function. Popping et al. (2019a) originally carried out the comparison with the observations by converting the L_{IR} to SFR following the relation in Murphy et al. (2011). Using the latter results in 0.16 dex lower L_{IR} for a fixed SFR than adopting Kennicutt (1998b), not changing the substance of our results. In every panel of Figures 4 and 5 the observed [C I] luminosities appear brighter than the predictions of the fiducial model at fixed L_{IR} . The observations seem to follow a steeper (shallower) trend than the model in the $L_{\text{IR}}-L_{[\text{C I}]^3 P_1 - ^3 P_0}$ ($L_{[\text{C I}]^3 P_2 - ^3 P_1}$) plane at $z \sim 0$, while the slope is similar at higher redshifts. Notice that this tension would increase if a substantial fraction of the total SFR is unobscured, reducing L_{IR} and moving the points towards the left. We register the minimal discrepancy between [C I] observations and models for the high-redshift SMGs in the $L_{\text{IR}}-L_{[\text{C I}]^3 P_2 - ^3 P_1}$ panel (Figure 5). On the contrary, the model successfully reproduces the CO (4–3) emission from local and main sequence galaxies at $z \sim 1$ (Figure 6). For reference, we also show the best fit $L_{\text{IR}}-L'_{\text{CO}(4-3)}$ relation from Liu et al. (2015). This is not surprising, considering the performances of the fiducial model for low- and mid- J CO transitions already reported by Popping et al. (2019a) for similar datasets. We draw similar conclusions for CO (5–4). On the contrary, the model overpredicts the $L'_{\text{CO}(4-3)}$ luminosity of high-redshift SMGs, which we find consistent with the -0.3 dex offset to the local relation (Liu et al. 2015; Yang et al. 2017).

The offset between the [C I] observations and the fiducial model, not corresponding to a displacement of the CO and [C II] measurements (Popping et al. 2019a, and references therein), suggests that the emission of neutral atomic carbon is not fully captured by the current recipes. We note that the sSFRs predicted by the Santa Cruz model do match the observed values for the massive star-forming population at $z = 0$, but the normalization of the main sequence falls below the empirical estimates at $z > 1$. This is a well known issue, as shown in Figure 11 from Somerville et al. (2015). Our sample of main sequence galaxies at $z \sim 1$ makes no exception: the observed median $\log(\text{sSFR}/\text{yr}^{-1}) = -9$ is larger than what is predicted by the model. However, the results of the comparison do not change even when limiting the model predictions to the star-forming population matching the observed sSFR threshold. On the other hand, the depletion timescales or SFEs are reasonably well described by the Santa Cruz model (Somerville et al. 2015; Popping et al. 2019b). Sys-

tematic differences in SFEs are unlikely to drive the discrepancy with the observations in Figures 4-6, since both [C I] and CO should have been similarly impacted. While further work on the model is necessary to remove the systematics on the sSFR, the relative comparison of CO and [C I] emission as a function of L_{IR} still holds. Therefore, the problem likely arises from the modeling of the emission itself.

Interestingly, the [C I] emission appears to be largely unaffected by several parameters, including the the density of the diffuse atomic ISM, the choice of rescaling the strength of the UV- and cosmic ray fields to the local or the global SFR, the slope of the molecular clouds distribution, the clumping of the ISM, and the radial density profile within the clouds at a fixed external pressure. On the contrary, the choice of the density profile within the molecular clouds might increase the $L_{[\text{C I}]^3 P_1 - ^3 P_0}$ at fixed SFR (Figure 9 in Popping et al. 2019a), also modifying the slope of the relation, as the observations suggest (Figures 4 and 5). Nevertheless, modifying only this parameter would generate tensions with the CO and [C II] observations that are currently indiscernible. We underline the fact that the model is meant to reproduce the bulk of the galaxy population. Therefore, strongly deviating outliers, such as starbursts and SMGs in the standard definitions and shown here for the sake of completeness, would likely require a specific treatment.

Further developments of these and alternative models appear necessary in order to reproduce the observations. The compilation we publicly release here will serve as a useful tool for calibration.

5. CONCLUSIONS

We presented new observations of [C I] ($^3 P_2 - ^3 P_1$) and CO (7–6) in a sample of 7 main sequence galaxies at $z \sim 1$, along with a compilation of > 200 objects with detected [C I] ($^3 P_1 - ^3 P_0$) and/or [C I] ($^3 P_2 - ^3 P_1$), and one or multiple low to high- J CO transitions. This compilation spans the $z = 0 - 4$ redshift interval and a wide range of ambient conditions. We leveraged such a large sample to derive the following results.

- The $L_{[\text{C I}]^3 P_1 - ^3 P_0}/L_{\text{IR}}$ and $L_{[\text{C I}]^3 P_2 - ^3 P_1}/L_{\text{IR}}$ ratios in local LIRGs and main sequence galaxies at $z \sim 1$ are consistent, but systematically and significantly higher than the values measured in SMGs at $z = 2 - 4$. We draw a similar conclusion for the $L_{[\text{C I}]^3 P_2 - ^3 P_1}/L_{\text{CO}(7-6)}$ ratio, while $L_{[\text{C I}]^3 P_1 - ^3 P_0}/L_{\text{CO}(4-3)}$ appears more consistent among the different redshifts and populations, re-

sembling the case of CO (2–1) previously reported in V18.

- The previous point can be interpreted considering that [C I], mid-/high- J CO ($J_{\text{upper}} = 3 - 7$), and L_{IR} trace the low density, high density molecular gas, and the SFR, respectively. The observed trends would thus suggest increased dense molecular gas fractions and higher SFEs in high-redshift SMGs than main sequence galaxies and local LIRGs, in agreement with CO-based studies. This is further consistent with the (integrated) Schmidt-Kennicutt relation and serves as supporting evidence of the potential of [C I] as an alternative molecular gas tracer.
- The observed $L'_{[\text{C I}]^3 P_2 - ^3 P_1} / L'_{[\text{C I}]^3 P_1 - ^3 P_0}$ ratios of the local, main sequence at $z \sim 1$ and high-redshift SMG samples are fully consistent. This suggests a similar gas temperature traced by [C I] across redshift and galaxy type.
- Moreover, the $L'_{[\text{C I}]^3 P_2 - ^3 P_1} / L'_{[\text{C I}]^3 P_1 - ^3 P_0}$ ratio ($\propto T_{\text{exc}}$) mildly correlates with $L'_{\text{CO}(7-6)} / L'_{\text{CO}(1-0)}$, a proxy for the shape of the CO SLED. More extreme excitation for [C I] corresponds to similar conditions of CO, supporting the coexistence of these molecular gas tracers.
- We find $T_{\text{exc}} \lesssim T_{\text{dust}}$ on global scales for the galaxies in our compilation and a mild correlation between these two quantities for local galaxies, but no apparent strong connection in the high-redshift sample. This might be due to the presence of multi-phased ISM and dust, with [C I] tracing a cold and extended component and the (luminosity-weighted) T_{dust} from the SED modeling being mainly driven by hot dust, not accounting for the bulk of the dust mass in the cold phase. However, this result critically depends on the modeling and parametrization of the far-IR SED and on relatively small number statistics of galaxies with both [C I] lines available, especially at high redshift.
- We fitted the observed line ratios using classical one-dimensional photodissociation region models (Kaufman et al. 1999), retrieving similar n, G_0 for local LIRGs and main sequence galaxies at $z \sim 1$, but larger values for high-redshift SMGs, consistent with the conclusions reported above.
- While valuable for a simple interpretation and relative comparisons among spatially unresolved observations, classical 1D PDR modeling is hampered by several shortcomings. Here we explored

the impact of using different combinations of line ratios, finding the necessity of a more comprehensive approach in order to reproduce a likely complex and multi-phased ISM at any redshifts. This adds to other well known issues previously reported.

- We compared our compilation with available semi-analytical models (Popping et al. 2019a) in order to place [C I] in a context of cosmological galaxy evolution. While we confirm a good agreement with fiducial model for the CO emission, we find systematically larger [C I] luminosities at fixed L_{IR} for any sample at any redshifts than the theoretical predictions. This suggests the necessity of a revision of some of the subgrid recipes assumed in the model.
- We release the data compilation in an electronic format to the community as a benchmark for future testing and comparison.

ACKNOWLEDGEMENTS

We acknowledge the constructive comments from the anonymous referee, which helped improving this work. We thank Mark Sargent and Anna Cibinel for providing the initial catalogs for the selection of main sequence galaxies. We thank Nathan Bourne, Fabian Walter and Axel Weiß for providing the photometry and line emission for their samples. FV thanks Qian Jiao for clarifying details of her work and sharing her data; Diane Cormier for discussions about the PDR modeling. FV and GEM acknowledge the Villum Fonden research grant 13160 “Gas to stars, stars to dust: tracing star formation across cosmic time” and the Cosmic Dawn Center of Excellence funded by the Danish National Research Foundation under then grant No. 140. FV acknowledges support from the Carlsberg Foundation research grant CF18-0388 “Galaxies: Rise And Death”. GEM acknowledges support from the European Research Council (ERC) Consolidator Grant funding scheme (project ConTExt, grant number 648179). SJ acknowledges financial support from the Spanish Ministry of Science, Innovation and Universities (MICIU) under grant AYA2017-84061-P, co-financed by FEDER (European Regional Development Funds). DL acknowledges funding from the European Research Council (ERC) under the European Union’s Horizon 2020 research and innovation programme (grant agreement No. 694343). YG’s research is supported by National Key Basic Research and Development Program of China (grant No. 2017YFA0402704), National Natural Science Founda-

tion of China (grant Nos. 11861131007, 11420101002), and Chinese Academy of Sciences Key Research Program of Frontier Sciences (grant No. QYZDJSSW-SLH008). In this work we made use of STSDAS. STSDAS is a product of the Space Telescope Science Institute, which is operated by AURA for NASA. This paper makes use of the following ALMA data: ADS/JAO.ALMA, #2018.1.00635.S, #2016.1.01040.S, #2016.1.00171.S, #2015.1.00260.S. ALMA is a part-

nership of ESO (representing its member states), NSF (USA) and NINS (Japan), together with NRC (Canada), MOST and ASIAA (Taiwan), and KASI (Republic of Korea), in cooperation with the Republic of Chile. The Joint ALMA Observatory is operated by ESO, AUI/NRAO and NAOJ. In this work we made use of the COSMOS master spectroscopic catalog, available within the collaboration and kept updated by Mara Salvato.

REFERENCES

- Alaghband-Zadeh, S., Chapman, S. C., Swinbank, A. M., et al. 2013, *MNRAS*, 435, 1493, doi: [10.1093/mnras/stt1390](https://doi.org/10.1093/mnras/stt1390)
- Andreani, P., Retana-Montenegro, E., Zhang, Z.-Y., et al. 2018, *A&A*, 615, A142, doi: [10.1051/0004-6361/201732560](https://doi.org/10.1051/0004-6361/201732560)
- Apostolovski, Y., Aravena, M., Anguita, T., et al. 2019, *A&A*, 628, A23, doi: [10.1051/0004-6361/201935308](https://doi.org/10.1051/0004-6361/201935308)
- Aravena, M., Spilker, J. S., Bethermin, M., et al. 2016, *MNRAS*, 457, 4406, doi: [10.1093/mnras/stw275](https://doi.org/10.1093/mnras/stw275)
- Armus, L., Mazzarella, J. M., Evans, A. S., et al. 2009, *PASP*, 121, 559, doi: [10.1086/600092](https://doi.org/10.1086/600092)
- Avni, Y. 1976, *ApJ*, 210, 642, doi: [10.1086/154870](https://doi.org/10.1086/154870)
- Bianchi, S. 2013, *A&A*, 552, A89, doi: [10.1051/0004-6361/201220866](https://doi.org/10.1051/0004-6361/201220866)
- Bisbas, T. G., Bell, T. A., Viti, S., Yates, J., & Barlow, M. J. 2012, *MNRAS*, 427, 2100, doi: [10.1111/j.1365-2966.2012.22077.x](https://doi.org/10.1111/j.1365-2966.2012.22077.x)
- Bisbas, T. G., Papadopoulos, P. P., & Viti, S. 2015, *ApJ*, 803, 37, doi: [10.1088/0004-637X/803/1/37](https://doi.org/10.1088/0004-637X/803/1/37)
- Bisbas, T. G., van Dishoeck, E. F., Papadopoulos, P. P., et al. 2017, *ApJ*, 839, 90, doi: [10.3847/1538-4357/aa696d](https://doi.org/10.3847/1538-4357/aa696d)
- Blain, A. W., Barnard, V. E., & Chapman, S. C. 2003, *MNRAS*, 338, 733, doi: [10.1046/j.1365-8711.2003.06086.x](https://doi.org/10.1046/j.1365-8711.2003.06086.x)
- Bolatto, A. D., Wolfire, M., & Leroy, A. K. 2013, *ARA&A*, 51, 207, doi: [10.1146/annurev-astro-082812-140944](https://doi.org/10.1146/annurev-astro-082812-140944)
- Bothwell, M. S., Smail, I., Chapman, S. C., et al. 2013, *MNRAS*, 429, 3047, doi: [10.1093/mnras/sts562](https://doi.org/10.1093/mnras/sts562)
- Bothwell, M. S., Aguirre, J. E., Aravena, M., et al. 2017, *MNRAS*, 466, 2825, doi: [10.1093/mnras/stw3270](https://doi.org/10.1093/mnras/stw3270)
- Bourne, N., Dunlop, J. S., Simpson, J. M., et al. 2019, *MNRAS*, 482, 3135, doi: [10.1093/mnras/sty2773](https://doi.org/10.1093/mnras/sty2773)
- Bourne, N., Dunlop, J. S., Merlin, E., et al. 2017, *MNRAS*, 467, 1360, doi: [10.1093/mnras/stx031](https://doi.org/10.1093/mnras/stx031)
- Brisbin, D., Aravena, M., Daddi, E., et al. 2019, arXiv e-prints, arXiv:1907.04936, <https://arxiv.org/abs/1907.04936>
- Bussmann, R. S., Pérez-Fournon, I., Amber, S., et al. 2013, *ApJ*, 779, 25, doi: [10.1088/0004-637X/779/1/25](https://doi.org/10.1088/0004-637X/779/1/25)
- Cañameras, R., Nesvadba, N. P. H., Guery, D., et al. 2015, *A&A*, 581, A105, doi: [10.1051/0004-6361/201425128](https://doi.org/10.1051/0004-6361/201425128)
- Cañameras, R., Yang, C., Nesvadba, N. P. H., et al. 2018, *A&A*, 620, A61, doi: [10.1051/0004-6361/201833625](https://doi.org/10.1051/0004-6361/201833625)
- Carilli, C. L., & Walter, F. 2013, *ARA&A*, 51, 105, doi: [10.1146/annurev-astro-082812-140953](https://doi.org/10.1146/annurev-astro-082812-140953)
- Casey, C. M., Narayanan, D., & Cooray, A. 2014, *PhR*, 541, 45, doi: [10.1016/j.physrep.2014.02.009](https://doi.org/10.1016/j.physrep.2014.02.009)
- Casey, C. M., Chapman, S. C., Daddi, E., et al. 2009, *MNRAS*, 400, 670, doi: [10.1111/j.1365-2966.2009.15517.x](https://doi.org/10.1111/j.1365-2966.2009.15517.x)
- Chabrier, G. 2003, *PASP*, 115, 763, doi: [10.1086/376392](https://doi.org/10.1086/376392)
- Coogan, R. T., Daddi, E., Sargent, M. T., et al. 2018, *MNRAS*, 479, 703, doi: [10.1093/mnras/sty1446](https://doi.org/10.1093/mnras/sty1446)
- Cortzen, I., Garrett, J., Magdis, G., et al. 2019, *MNRAS*, 482, 1618, doi: [10.1093/mnras/sty2777](https://doi.org/10.1093/mnras/sty2777)
- da Cunha, E., Groves, B., Walter, F., et al. 2013, *ApJ*, 766, 13, doi: [10.1088/0004-637X/766/1/13](https://doi.org/10.1088/0004-637X/766/1/13)
- Daddi, E., Dickinson, M., Morrison, G., et al. 2007, *ApJ*, 670, 156, doi: [10.1086/521818](https://doi.org/10.1086/521818)
- Daddi, E., Dannerbauer, H., Stern, D., et al. 2009, *ApJ*, 694, 1517, doi: [10.1088/0004-637X/694/2/1517](https://doi.org/10.1088/0004-637X/694/2/1517)
- Daddi, E., Elbaz, D., Walter, F., et al. 2010, *ApJL*, 714, L118, doi: [10.1088/2041-8205/714/1/L118](https://doi.org/10.1088/2041-8205/714/1/L118)
- Daddi, E., Dannerbauer, H., Liu, D., et al. 2015, *A&A*, 577, A46, doi: [10.1051/0004-6361/201425043](https://doi.org/10.1051/0004-6361/201425043)
- Dale, D. A., Aniano, G., Engelbracht, C. W., et al. 2012, *ApJ*, 745, 95, doi: [10.1088/0004-637X/745/1/95](https://doi.org/10.1088/0004-637X/745/1/95)
- Danielson, A. L. R., Swinbank, A. M., Smail, I., et al. 2011, *MNRAS*, 410, 1687, doi: [10.1111/j.1365-2966.2010.17549.x](https://doi.org/10.1111/j.1365-2966.2010.17549.x)
- Dannerbauer, H., Harrington, K., Díaz-Sánchez, A., et al. 2019, *AJ*, 158, 34, doi: [10.3847/1538-3881/aaf50b](https://doi.org/10.3847/1538-3881/aaf50b)
- Davies, R. I., Sternberg, A., Lehnert, M., & Tacconi-Garman, L. E. 2003, *ApJ*, 597, 907, doi: [10.1086/378634](https://doi.org/10.1086/378634)

- Díaz-Sánchez, A., Iglesias-Groth, S., Rebolo, R., & Dannerbauer, H. 2017, *ApJL*, 843, L22, doi: [10.3847/2041-8213/aa79ef](https://doi.org/10.3847/2041-8213/aa79ef)
- Donley, J. L., Koekemoer, A. M., Brusa, M., et al. 2012, *ApJ*, 748, 142, doi: [10.1088/0004-637X/748/2/142](https://doi.org/10.1088/0004-637X/748/2/142)
- Draine, B. T., & Li, A. 2007, *ApJ*, 657, 810, doi: [10.1086/511055](https://doi.org/10.1086/511055)
- Eales, S., Dunne, L., Clements, D., et al. 2010, *PASP*, 122, 499, doi: [10.1086/653086](https://doi.org/10.1086/653086)
- Elbaz, D., Daddi, E., Le Borgne, D., et al. 2007, *A&A*, 468, 33, doi: [10.1051/0004-6361:20077525](https://doi.org/10.1051/0004-6361:20077525)
- Feigelson, E. D., & Nelson, P. I. 1985, *ApJ*, 293, 192, doi: [10.1086/163225](https://doi.org/10.1086/163225)
- Galliano, F., Hony, S., Bernard, J. P., et al. 2011, *A&A*, 536, A88, doi: [10.1051/0004-6361/201117952](https://doi.org/10.1051/0004-6361/201117952)
- Gao, Y., Carilli, C. L., Solomon, P. M., & Vand en Bout, P. A. 2007, *ApJL*, 660, L93, doi: [10.1086/518244](https://doi.org/10.1086/518244)
- Gao, Y., & Solomon, P. M. 1999, *ApJL*, 512, L99, doi: [10.1086/311878](https://doi.org/10.1086/311878)
- . 2004, *ApJ*, 606, 271, doi: [10.1086/382999](https://doi.org/10.1086/382999)
- Geach, J. E., Dunlop, J. S., Halpern, M., et al. 2017, *MNRAS*, 465, 1789, doi: [10.1093/mnras/stw2721](https://doi.org/10.1093/mnras/stw2721)
- Genzel, R., Tacconi, L. J., Lutz, D., et al. 2015, *ApJ*, 800, 20, doi: [10.1088/0004-637X/800/1/20](https://doi.org/10.1088/0004-637X/800/1/20)
- Gerin, M., & Phillips, T. G. 2000, *ApJ*, 537, 644, doi: [10.1086/309072](https://doi.org/10.1086/309072)
- Glover, S. C. O., Clark, P. C., Micic, M., & Molina, F. 2015, *MNRAS*, 448, 1607, doi: [10.1093/mnras/stu2699](https://doi.org/10.1093/mnras/stu2699)
- Gómez-Guijarro, C., Magdis, G. E., Valentino, F., et al. 2019, arXiv e-prints, arXiv:1909.02572. <https://arxiv.org/abs/1909.02572>
- Greve, T. R., Leonidaki, I., Xilouris, E. M., et al. 2014, *ApJ*, 794, 142, doi: [10.1088/0004-637X/794/2/142](https://doi.org/10.1088/0004-637X/794/2/142)
- Guilloteau, S., & Lucas, R. 2000, in *Astronomical Society of the Pacific Conference Series*, Vol. 217, *Imaging at Radio through Submillimeter Wavelengths*, ed. J. G. Mangum & S. J. E. Radford, 299
- Gullberg, B., De Breuck, C., Vieira, J. D., et al. 2015, *MNRAS*, 449, 2883, doi: [10.1093/mnras/stv372](https://doi.org/10.1093/mnras/stv372)
- Gullberg, B., Lehnert, M. D., De Breuck, C., et al. 2016, *A&A*, 591, A73, doi: [10.1051/0004-6361/201527647](https://doi.org/10.1051/0004-6361/201527647)
- Habing, H. J. 1968, *BAN*, 19, 421
- Harrington, K. C., Yun, M. S., Magnelli, B., et al. 2018, *MNRAS*, 474, 3866, doi: [10.1093/mnras/stx3043](https://doi.org/10.1093/mnras/stx3043)
- Harris, A. I., Baker, A. J., Frayer, D. T., et al. 2012, *ApJ*, 752, 152, doi: [10.1088/0004-637X/752/2/152](https://doi.org/10.1088/0004-637X/752/2/152)
- Ikeda, M., Oka, T., Tatematsu, K., Sekimoto, Y., & Yamamoto, S. 2002, *ApJS*, 139, 467, doi: [10.1086/338761](https://doi.org/10.1086/338761)
- Israel, F. P., Rosenberg, M. J. F., & van der Werf, P. 2015, *A&A*, 578, A95, doi: [10.1051/0004-6361/201425175](https://doi.org/10.1051/0004-6361/201425175)
- Ivison, R. J., Swinbank, A. M., Swinyard, B., et al. 2010, *A&A*, 518, L35, doi: [10.1051/0004-6361/201014548](https://doi.org/10.1051/0004-6361/201014548)
- Jiao, Q., Zhao, Y., Zhu, M., et al. 2017, *ApJL*, 840, L18, doi: [10.3847/2041-8213/aa6f0f](https://doi.org/10.3847/2041-8213/aa6f0f)
- Jiao, Q., Zhao, Y., Lu, N., et al. 2019a, arXiv e-prints, arXiv:1906.05671. <https://arxiv.org/abs/1906.05671>
- . 2019b, *ApJ*, 883, 207, doi: [10.3847/1538-4357/ab44cc](https://doi.org/10.3847/1538-4357/ab44cc)
- Jin, S., Daddi, E., Liu, D., et al. 2018, *ApJ*, 864, 56, doi: [10.3847/1538-4357/aad4af](https://doi.org/10.3847/1538-4357/aad4af)
- Jin, S., Daddi, E., Magdis, G. E., et al. 2019, arXiv e-prints, arXiv:1906.00040. <https://arxiv.org/abs/1906.00040>
- Jones, S. F., 2015, PhD thesis, Univ. Leicester, doi: <https://core.ac.uk/download/pdf/42018134.pdf>
- Kamenetzky, J., Rangwala, N., Glenn, J., Maloney, P. R., & Conley, A. 2016, *ApJ*, 829, 93, doi: [10.3847/0004-637X/829/2/93](https://doi.org/10.3847/0004-637X/829/2/93)
- Kaplan, E. L., & Meier, P. 1958, *J. Am. Stat. Assoc.*, 53, 282, doi: [10.2307/2281868](https://doi.org/10.2307/2281868)
- Kaufman, M. J., Wolfire, M. G., & Hollenbach, D. J. 2006, *ApJ*, 644, 283, doi: [10.1086/503596](https://doi.org/10.1086/503596)
- Kaufman, M. J., Wolfire, M. G., Hollenbach, D. J., & Luhman, M. L. 1999, *ApJ*, 527, 795, doi: [10.1086/308102](https://doi.org/10.1086/308102)
- Keene, J., Lis, D. C., Phillips, T. G., & Schilke, P. 1996, in *IAU Symposium*, Vol. 178, *Molecules in Astrophysics: Probes & Processes*, ed. E. F. van Dishoeck, 129
- Kennicutt, Jr., R. C. 1998a, *ApJ*, 498, 541
- . 1998b, *ARA&A*, 36, 189, doi: [10.1146/annurev.astro.36.1.189](https://doi.org/10.1146/annurev.astro.36.1.189)
- Krumholz, M. R. 2014, *MNRAS*, 437, 1662, doi: [10.1093/mnras/stt2000](https://doi.org/10.1093/mnras/stt2000)
- Laigle, C., McCracken, H. J., Ilbert, O., et al. 2016, *ApJS*, 224, 24, doi: [10.3847/0067-0049/224/2/24](https://doi.org/10.3847/0067-0049/224/2/24)
- Lamarche, C., Stacey, G. J., Vishwas, A., et al. 2019, *ApJ*, 882, 1, doi: [10.3847/1538-4357/ab3389](https://doi.org/10.3847/1538-4357/ab3389)
- Lee, M.-Y., Madden, S., Le Petit, F., et al. 2019, arXiv e-prints, arXiv:1905.10051. <https://arxiv.org/abs/1905.10051>
- Lelli, F., De Breuck, C., Falkendal, T., et al. 2018, *MNRAS*, 479, 5440, doi: [10.1093/mnras/sty1795](https://doi.org/10.1093/mnras/sty1795)
- Liang, L., Feldmann, R., Kereš, D., et al. 2019, arXiv e-prints, arXiv:1902.10727. <https://arxiv.org/abs/1902.10727>
- Liu, D., Gao, Y., Isaak, K., et al. 2015, *ApJL*, 810, L14, doi: [10.1088/2041-8205/810/2/L14](https://doi.org/10.1088/2041-8205/810/2/L14)
- Liu, D., Lang, P., Magnelli, B., et al. 2019, *ApJS*, 244, 40, doi: [10.3847/1538-4365/ab42da](https://doi.org/10.3847/1538-4365/ab42da)
- Lu, N., Zhao, Y., Xu, C. K., et al. 2015, *ApJL*, 802, L11, doi: [10.1088/2041-8205/802/1/L11](https://doi.org/10.1088/2041-8205/802/1/L11)
- Lu, N., Zhao, Y., Díaz-Santos, T., et al. 2017, *ApJS*, 230, 1, doi: [10.3847/1538-4365/aa6476](https://doi.org/10.3847/1538-4365/aa6476)

- Lutz, D., Poglitsch, A., Altieri, B., et al. 2011, *A&A*, 532, A90, doi: [10.1051/0004-6361/201117107](https://doi.org/10.1051/0004-6361/201117107)
- Magdis, G. E., Rigopoulou, D., Huang, J. S., & Fazio, G. G. 2010, *MNRAS*, 401, 1521, doi: [10.1111/j.1365-2966.2009.15779.x](https://doi.org/10.1111/j.1365-2966.2009.15779.x)
- Magdis, G. E., Daddi, E., Béthermin, M., et al. 2012a, *ApJ*, 760, 6, doi: [10.1088/0004-637X/760/1/6](https://doi.org/10.1088/0004-637X/760/1/6)
- . 2012b, *ApJ*, 760, 6, doi: [10.1088/0004-637X/760/1/6](https://doi.org/10.1088/0004-637X/760/1/6)
- Magdis, G. E., Rigopoulou, D., Daddi, E., et al. 2017, *A&A*, 603, A93, doi: [10.1051/0004-6361/201731037](https://doi.org/10.1051/0004-6361/201731037)
- Malhotra, S., Kaufman, M. J., Hollenbach, D., et al. 2001, *ApJ*, 561, 766, doi: [10.1086/323046](https://doi.org/10.1086/323046)
- Man, A. W. S., Lehnert, M. D., Vernet, J. D. R., De Breuck, C., & Falkendal, T. 2019, *A&A*, 624, A81, doi: [10.1051/0004-6361/201834542](https://doi.org/10.1051/0004-6361/201834542)
- Markwardt, C. B. 2009, in *Astronomical Society of the Pacific Conference Series*, Vol. 411, *Astronomical Data Analysis Software and Systems XVIII*, ed. D. A. Bohlender, D. Durand, & P. Dowler, 251. <https://arxiv.org/abs/0902.2850>
- McMullin, J. P., Waters, B., Schiebel, D., Young, W., & Golap, K. 2007, in *Astronomical Society of the Pacific Conference Series*, Vol. 376, *Astronomical Data Analysis Software and Systems XVI*, ed. R. A. Shaw, F. Hill, & D. J. Bell, 127
- Meijerink, R., Spaans, M., & Israel, F. P. 2007, *A&A*, 461, 793, doi: [10.1051/0004-6361:20066130](https://doi.org/10.1051/0004-6361:20066130)
- Momcheva, I. G., Brammer, G. B., van Dokkum, P. G., et al. 2016, *ApJS*, 225, 27, doi: [10.3847/0067-0049/225/2/27](https://doi.org/10.3847/0067-0049/225/2/27)
- Mullaney, J. R., Alexander, D. M., Goulding, A. D., & Hickox, R. C. 2011, *MNRAS*, 414, 1082, doi: [10.1111/j.1365-2966.2011.18448.x](https://doi.org/10.1111/j.1365-2966.2011.18448.x)
- Murphy, E. J., Condon, J. J., Schinnerer, E., et al. 2011, *ApJ*, 737, 67, doi: [10.1088/0004-637X/737/2/67](https://doi.org/10.1088/0004-637X/737/2/67)
- Muzzin, A., Wilson, G., Demarco, R., et al. 2013, *ApJ*, 767, 39, doi: [10.1088/0004-637X/767/1/39](https://doi.org/10.1088/0004-637X/767/1/39)
- Narayanan, D., & Krumholz, M. R. 2017, *MNRAS*, 467, 50, doi: [10.1093/mnras/stw3218](https://doi.org/10.1093/mnras/stw3218)
- Negrello, M., Hopwood, R., De Zotti, G., et al. 2010, *Science*, 330, 800, doi: [10.1126/science.1193420](https://doi.org/10.1126/science.1193420)
- Nesvadba, N., Canameras, R., Kneissl, R., et al. 2018, arXiv e-prints. <https://arxiv.org/abs/1812.04653>
- Noeske, K. G., Weiner, B. J., Faber, S. M., et al. 2007, *ApJL*, 660, L43, doi: [10.1086/517926](https://doi.org/10.1086/517926)
- Ojha, R., Stark, A. A., Hsieh, H. H., et al. 2001, *ApJ*, 548, 253, doi: [10.1086/318693](https://doi.org/10.1086/318693)
- Olsen, K., Pallottini, A., Wofford, A., et al. 2018, *Galaxies*, 6, 100, doi: [10.3390/galaxies6040100](https://doi.org/10.3390/galaxies6040100)
- Papadopoulos, P. P., Bisbas, T. G., & Zhang, Z.-Y. 2018, *MNRAS*, 478, 1716, doi: [10.1093/mnras/sty1077](https://doi.org/10.1093/mnras/sty1077)
- Papadopoulos, P. P., Thi, W.-F., & Viti, S. 2004, *MNRAS*, 351, 147, doi: [10.1111/j.1365-2966.2004.07762.x](https://doi.org/10.1111/j.1365-2966.2004.07762.x)
- Popping, G., Narayanan, D., Somerville, R. S., Faisst, A. L., & Krumholz, M. R. 2019a, *MNRAS*, 482, 4906, doi: [10.1093/mnras/sty2969](https://doi.org/10.1093/mnras/sty2969)
- Popping, G., Somerville, R. S., & Trager, S. C. 2014, *MNRAS*, 442, 2398, doi: [10.1093/mnras/stu991](https://doi.org/10.1093/mnras/stu991)
- Popping, G., Decarli, R., Man, A. W. S., et al. 2017, *A&A*, 602, A11, doi: [10.1051/0004-6361/201730391](https://doi.org/10.1051/0004-6361/201730391)
- Popping, G., Pillepich, A., Somerville, R. S., et al. 2019b, *ApJ*, 882, 137, doi: [10.3847/1538-4357/ab30f2](https://doi.org/10.3847/1538-4357/ab30f2)
- Pound, M. W., & Wolfire, M. G. 2008, in *Astronomical Society of the Pacific Conference Series*, Vol. 394, *Astronomical Data Analysis Software and Systems XVII*, ed. R. W. Argyle, P. S. Bunclark, & J. R. Lewis, 654
- Puglisi, A., Daddi, E., Liu, D., et al. 2019, *ApJ*, 877, L23, doi: [10.3847/2041-8213/ab1f92](https://doi.org/10.3847/2041-8213/ab1f92)
- Sanders, D. B., Mazzarella, J. M., Kim, D.-C., Surace, J. A., & Soifer, B. T. 2003, *AJ*, 126, 1607, doi: [10.1086/376841](https://doi.org/10.1086/376841)
- Schmidt, M. 1959, *ApJ*, 129, 243
- Schneider, N., Simon, R., Kramer, C., et al. 2003, *A&A*, 406, 915, doi: [10.1051/0004-6361:20030726](https://doi.org/10.1051/0004-6361:20030726)
- Schreiber, C., Elbaz, D., Pannella, M., et al. 2018, *A&A*, 609, A30, doi: [10.1051/0004-6361/201731506](https://doi.org/10.1051/0004-6361/201731506)
- Scoville, N., Aussel, H., Brusa, M., et al. 2007, *ApJS*, 172, 1, doi: [10.1086/516585](https://doi.org/10.1086/516585)
- Scoville, N., Aussel, H., Sheth, K., et al. 2014, *ApJ*, 783, 84, doi: [10.1088/0004-637X/783/2/84](https://doi.org/10.1088/0004-637X/783/2/84)
- Skelton, R. E., Whitaker, K. E., Momcheva, I. G., et al. 2014, *ApJS*, 214, 24, doi: [10.1088/0067-0049/214/2/24](https://doi.org/10.1088/0067-0049/214/2/24)
- Solomon, P. M., Downes, D., Radford, S. J. E., & Barrett, J. W. 1997, *ApJ*, 478, 144, doi: [10.1086/303765](https://doi.org/10.1086/303765)
- Somerville, R. S., Popping, G., & Trager, S. C. 2015, *MNRAS*, 453, 4337, doi: [10.1093/mnras/stv1877](https://doi.org/10.1093/mnras/stv1877)
- Somerville, R. S., & Primack, J. R. 1999, *MNRAS*, 310, 1087, doi: [10.1046/j.1365-8711.1999.03032.x](https://doi.org/10.1046/j.1365-8711.1999.03032.x)
- Somerville, R. S., Primack, J. R., & Faber, S. M. 2001, *MNRAS*, 320, 504, doi: [10.1046/j.1365-8711.2001.03975.x](https://doi.org/10.1046/j.1365-8711.2001.03975.x)
- Stacey, G. J., Geis, N., Genzel, R., et al. 1991, *ApJ*, 373, 423, doi: [10.1086/170062](https://doi.org/10.1086/170062)
- Stoerzer, H., Stutzki, J., & Sternberg, A. 1997, *A&A*, 323, L13
- Strandet, M. L., Weiss, A., De Breuck, C., et al. 2017, *ApJL*, 842, L15, doi: [10.3847/2041-8213/aa74b0](https://doi.org/10.3847/2041-8213/aa74b0)
- Stutzki, J., Bensch, F., Heithausen, A., Ossenkopf, V., & Zielinsky, M. 1998, *A&A*, 336, 697

- Stutzki, J., Graf, U. U., Haas, S., et al. 1997, *ApJL*, 477, L33, doi: [10.1086/310514](https://doi.org/10.1086/310514)
- Tacconi, L. J., Genzel, R., Saintonge, A., et al. 2018, *ApJ*, 853, 179, doi: [10.3847/1538-4357/aaa4b4](https://doi.org/10.3847/1538-4357/aaa4b4)
- Talia, M., Pozzi, F., Vallini, L., et al. 2018, *MNRAS*, 476, 3956, doi: [10.1093/mnras/sty481](https://doi.org/10.1093/mnras/sty481)
- Tielens, A. G. G. M., & Hollenbach, D. 1985, *ApJ*, 291, 722, doi: [10.1086/163111](https://doi.org/10.1086/163111)
- Valentino, F., Magdis, G. E., Daddi, E., et al. 2018, *ApJ*, 869, 27, doi: [10.3847/1538-4357/aaeb88](https://doi.org/10.3847/1538-4357/aaeb88)
- van Dokkum, P. G., Nelson, E. J., Franx, M., et al. 2015, *ApJ*, 813, 23, doi: [10.1088/0004-637X/813/1/23](https://doi.org/10.1088/0004-637X/813/1/23)
- Véron-Cetty, M.-P., & Véron, P. 2010, *A&A*, 518, A10, doi: [10.1051/0004-6361/201014188](https://doi.org/10.1051/0004-6361/201014188)
- Vieira, J. D., Crawford, T. M., Switzer, E. R., et al. 2010, *ApJ*, 719, 763, doi: [10.1088/0004-637X/719/1/763](https://doi.org/10.1088/0004-637X/719/1/763)
- Walter, F., Weiß, A., Downes, D., Decarli, R., & Henkel, C. 2011, *ApJ*, 730, 18, doi: [10.1088/0004-637X/730/1/18](https://doi.org/10.1088/0004-637X/730/1/18)
- Weiß, A., Downes, D., Henkel, C., & Walter, F. 2005, *A&A*, 429, L25, doi: [10.1051/0004-6361:200400085](https://doi.org/10.1051/0004-6361:200400085)
- Weiß, A., Henkel, C., Downes, D., & Walter, F. 2003, *A&A*, 409, L41, doi: [10.1051/0004-6361:20031337](https://doi.org/10.1051/0004-6361:20031337)
- Weiß, A., De Breuck, C., Marrone, D. P., et al. 2013, *ApJ*, 767, 88, doi: [10.1088/0004-637X/767/1/88](https://doi.org/10.1088/0004-637X/767/1/88)
- Xie, T., Allen, M., & Langer, W. D. 1995, *ApJ*, 440, 674, doi: [10.1086/175305](https://doi.org/10.1086/175305)
- Yamashita, T., Komugi, S., Matsuhara, H., et al. 2017, *ApJ*, 844, 96, doi: [10.3847/1538-4357/aa7af1](https://doi.org/10.3847/1538-4357/aa7af1)
- Yang, C., Omont, A., Beelen, A., et al. 2017, *A&A*, 608, A144, doi: [10.1051/0004-6361/201731391](https://doi.org/10.1051/0004-6361/201731391)
- Young, J. S., & Scoville, N. Z. 1991, *ARA&A*, 29, 581, doi: [10.1146/annurev.aa.29.090191.003053](https://doi.org/10.1146/annurev.aa.29.090191.003053)
- Zanella, A., Daddi, E., Magdis, G., et al. 2018, *MNRAS*, 481, 1976, doi: [10.1093/mnras/sty2394](https://doi.org/10.1093/mnras/sty2394)
- Zhang, Z.-Y., Papadopoulos, P. P., Ivison, R. J., et al. 2016, *Royal Society Open Science*, 3, 160025, doi: [10.1098/rsos.160025](https://doi.org/10.1098/rsos.160025)
- Zhang, Z.-Y., Ivison, R. J., George, R. D., et al. 2018, *MNRAS*, 481, 59, doi: [10.1093/mnras/sty2082](https://doi.org/10.1093/mnras/sty2082)

APPENDIX

A. SPECTRAL ENERGY DISTRIBUTION OF THE HIGH-REDSHIFT SAMPLE

As part of the supplementary online material, we show the re-modeling of the SED we performed for all the high-redshift galaxies from the literature samples that we collected (Figure 7). The SEDs of our own sample of main sequence galaxies are reported with an identical format in V18, excluding sources #208273 and 256703 included in this release. We do not show the SMG from Jin et al. (2019), being the modeling identical to the original work. In each panel, we show in red the photometric points we fitted and their uncertainties. Downpointing arrows indicate 2σ upper limits. Open red symbols mark photometry from *Spitzer*/IRAC and radio when available, which we did not use to constrain the fit. The black line shows the best composite SED (Draine & Li (2007) and AGN templates from Mullaney et al. (2011), the latter highlighted in blue).

B. TOTAL RECOVERED FLUXES FROM ALMA OBSERVATIONS

We extracted the flux of each line of our sample of main sequence galaxies using the iterative procedure described in detail in our previous work (Daddi et al. 2015; Coogan et al. 2018; Valentino et al. 2018; Puglisi et al. 2019) and recalled in Section 2.1.2. The signal is extracted with GILDAS/UV_FIT at fixed spatial position and extension, obtained by combining measurements for each tracer in the uv space (Section 2 of Puglisi et al. 2019). Such combination includes both cold ([C I], CO (2 – 1), dust continuum) and warm (CO (4 – 3), CO (5 – 4), CO (7 – 6)) molecular gas proxies. Therefore, the measured size is representative of the average extension of the molecular gas in the galaxy. Further comparisons between the various tracers is part of a forthcoming work (Puglisi et al. in prep.). The total flux is robustly recovered whenever the size of the emitting source is securely estimated. This is the case for all the new Band 7 measurements reported in Section 2.1.2. However, flux losses might occur when only an upper limit on the size can be placed, and such estimate is comparable with the beam size. We estimated these losses by injecting artificial bright galaxies with circular Gaussian profiles and a FWHM fixed to the 1σ upper limit on the size in the ALMA maps, and then re-extracting their fluxes with the fiducial point source profile. We corrected the fluxes of unresolved sources to $(I_{\text{Gauss}}/I_{\text{Point}} + 1)/2$ and adding in quadrature the absolute error on such correction ($\sigma_{\text{corr}} = (I_{\text{Gauss}} - I_{\text{Point}})/2$) to the statistical uncertainty. The sizes and the flux corrections are reported in Table 5. Changes at $< 5\%$ are not significant and therefore not applied.

C. DATA TABLES

The data we collected for this work are released in electronic FITS format available in the online version of the article or contacting the corresponding author. We produce two separate tables for the local and high-redshift subsamples in Section 2. The quantities are described in Table 6.

D. SPECTRA OF MAIN SEQUENCE GALAXIES

We show in Figure 9 the spectra of our sample of $z \sim 1.2$ main sequence galaxies observed with ALMA in Cycles 3 to 6 (Sections 2.1.1-V18 and 2.1.2). The IDs are reported in each panel and correspond to the ones in Tables 2 and 3. The black solid lines show the continuum-subtracted spectra in the observed frame and the red lines mark the best Gaussian fits. The black ticks signpost the expected line frequency from previous optical/near-IR redshift estimates. The shaded areas indicate the channels used to estimate the line fluxes. The number of channels covered by each line is reported in brackets. The spectra are color coded as follows: dark green = CO (2 – 1); blue = CO (4 – 3); yellow = [C I] ($^3P_1 - ^3P_0$), [C I] ($^3P_2 - ^3P_1$); orange = CO (5 – 4); purple = CO (7 – 6). In case of non-detections, we show the expected location of the emission with a red solid line, and the channels covered to estimate the upper limits on the flux as color shaded areas. These correspond to the velocity width of other significantly detected lines for the same source (Section 2.1.1).

E. TESTS ON PDR MODELING

In Section 4.1 we proposed a simple interpretation of the observed trends in the line ratios in terms of PDR modeling. As mentioned, this should be taken as an order of magnitude estimate, given the limitations of such a simple approach. Documented issues arise because of the simple one-dimensional geometry of classical PDR models, in which the [C I]

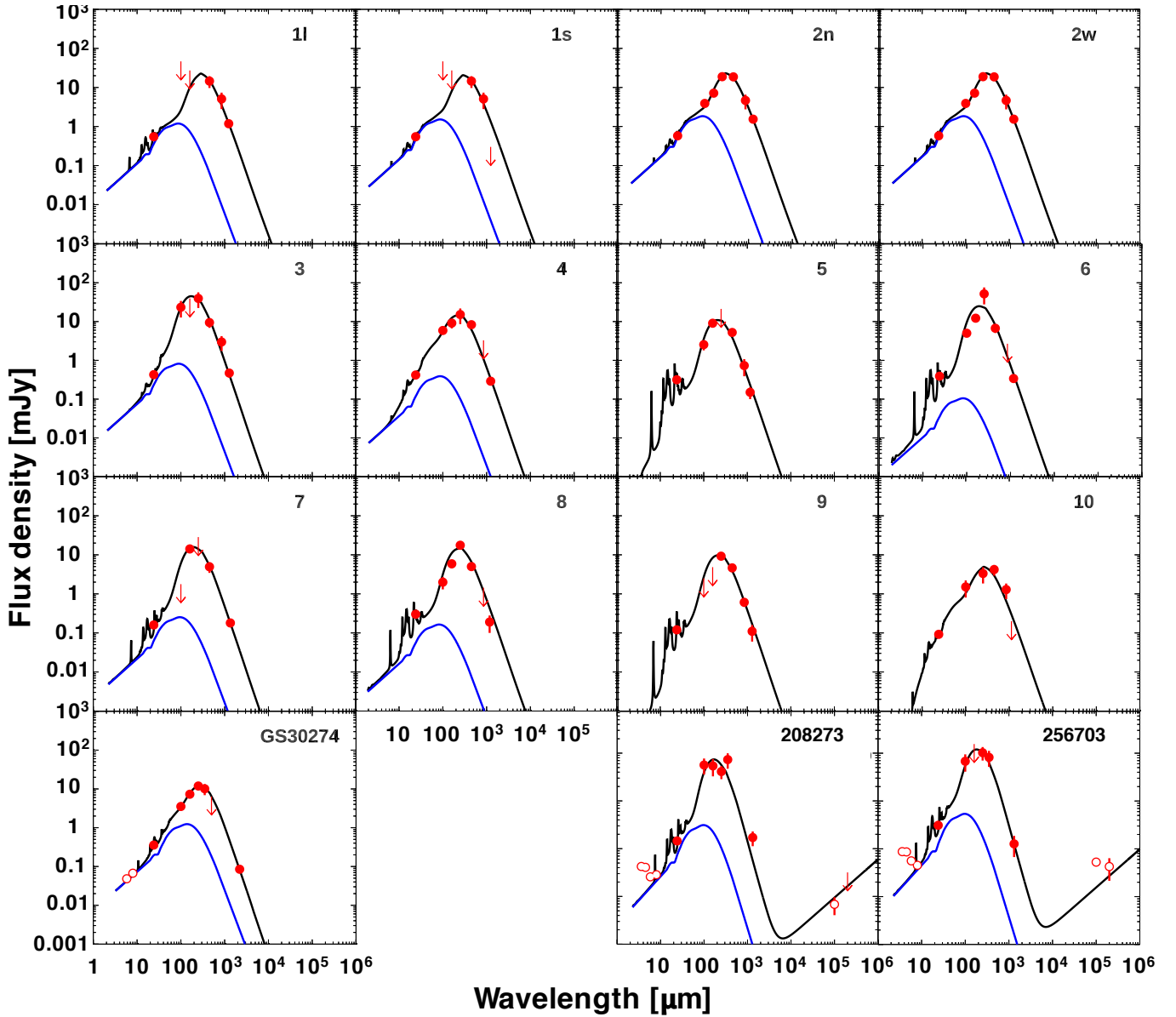


Figure 7. Far-infrared spectral energy distribution for the literature sample at high redshift. Red full circles mark the observed photometric points. Downpointing red arrows indicate 2σ upper limits. Open red symbols show photometry from *Spitzer*/IRAC and radio when available, not used in the fit. The black line shows the best composite SED (Draine & Li (2007) and AGN templates from Mullaney et al. (2011), the latter highlighted in blue). See Appendix A for details.

emission arises only from a thin layer within CO and [C II], while observations suggest full mixing between [C I] and CO (e.g., Ojha et al. 2001; Ikeda et al. 2002); the assumption of a micro turbulent medium, not suitable to reproduce the CO SLED, which is better represented by large velocity gradients (e.g., LVG modeling, Young & Scoville 1991; Liu et al. 2015; Yang et al. 2017; Cañameras et al. 2018 for working examples on subsets of the galaxies in our compilation); indeed, a clumpy medium, turbulent mixing and cosmic ray (rather FUV-) driven chemistry radically change this picture and might explain the fully concomitant [C I] and CO (e.g. Papadopoulos et al. 2004; Bisbas et al. 2015, 2017; Papadopoulos et al. 2018). More realistic modeling including a 3D geometry and tunable cosmic ray rates resulted in larger gas densities, but similar radiation fields with respect to the Kaufman et al. (1999) models adopted here (Bothwell et al. 2017). The mechanical excitation of CO transitions through shocks is known to occur in nearby massively star forming regions and it adds a further layer of complexity not captured by the simple PDR models we applied (Lee et al. 2019). We also note that metallicity and carbon abundance variations among different populations

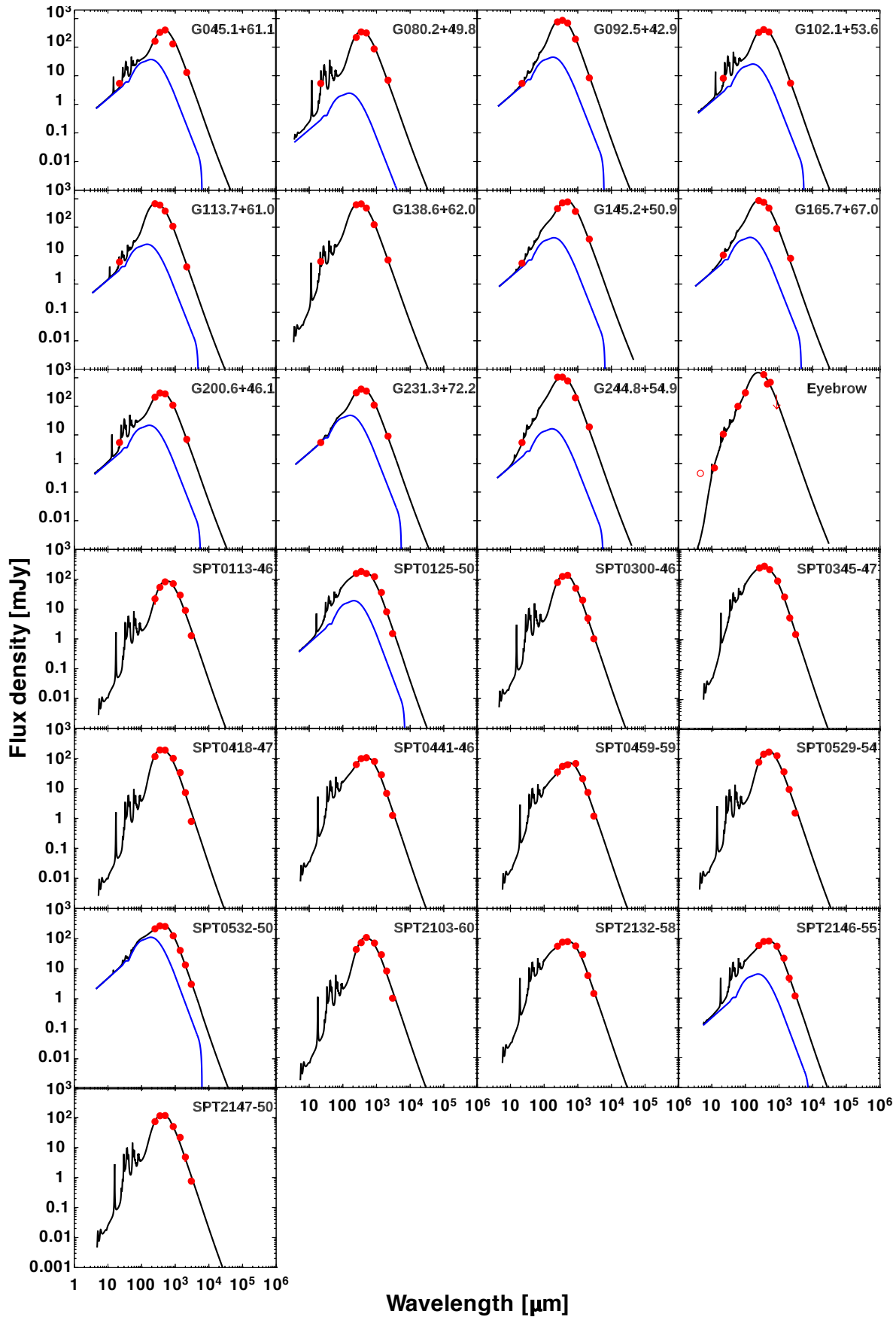


Figure 7. (continue)

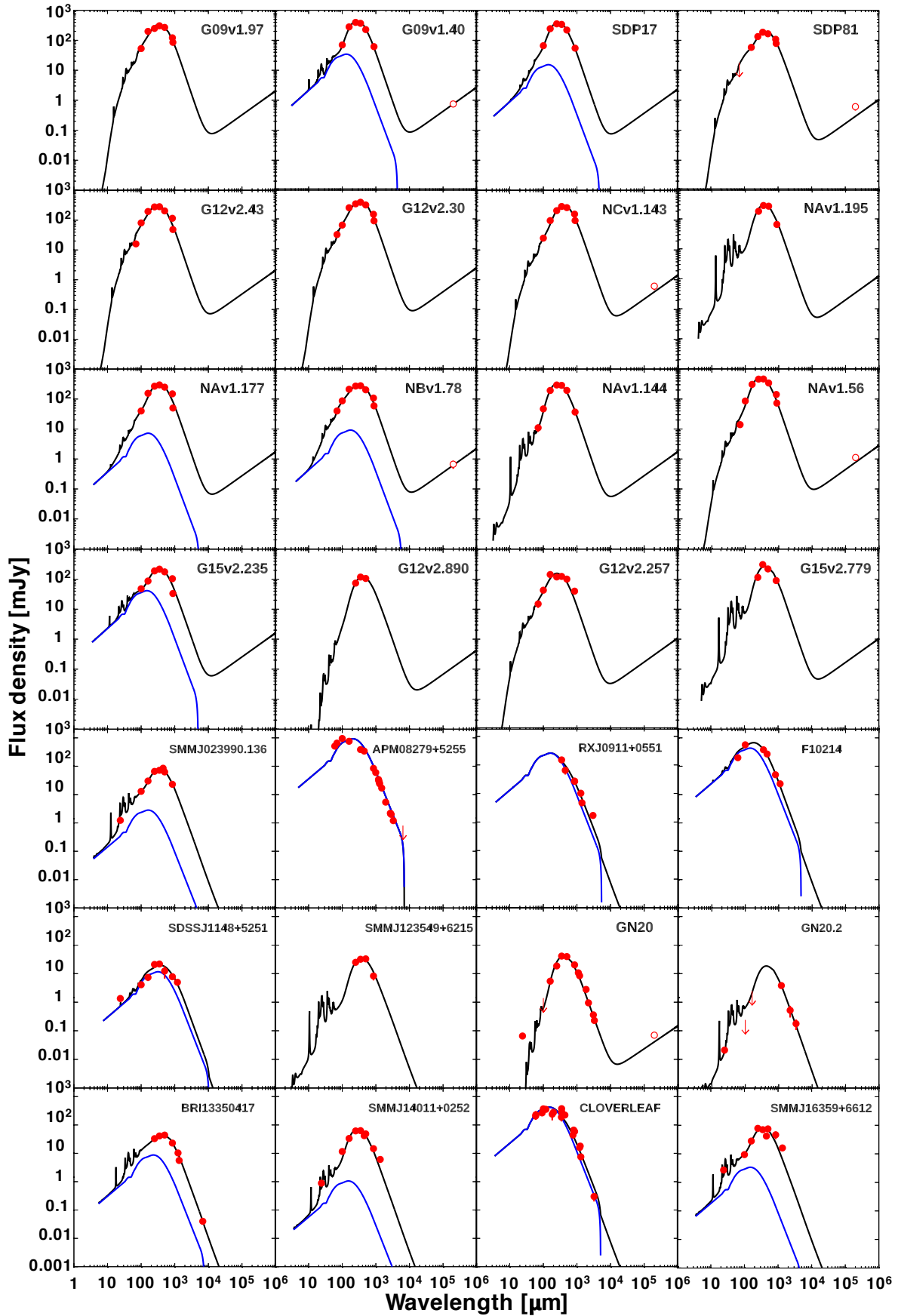


Figure 7. (continue)

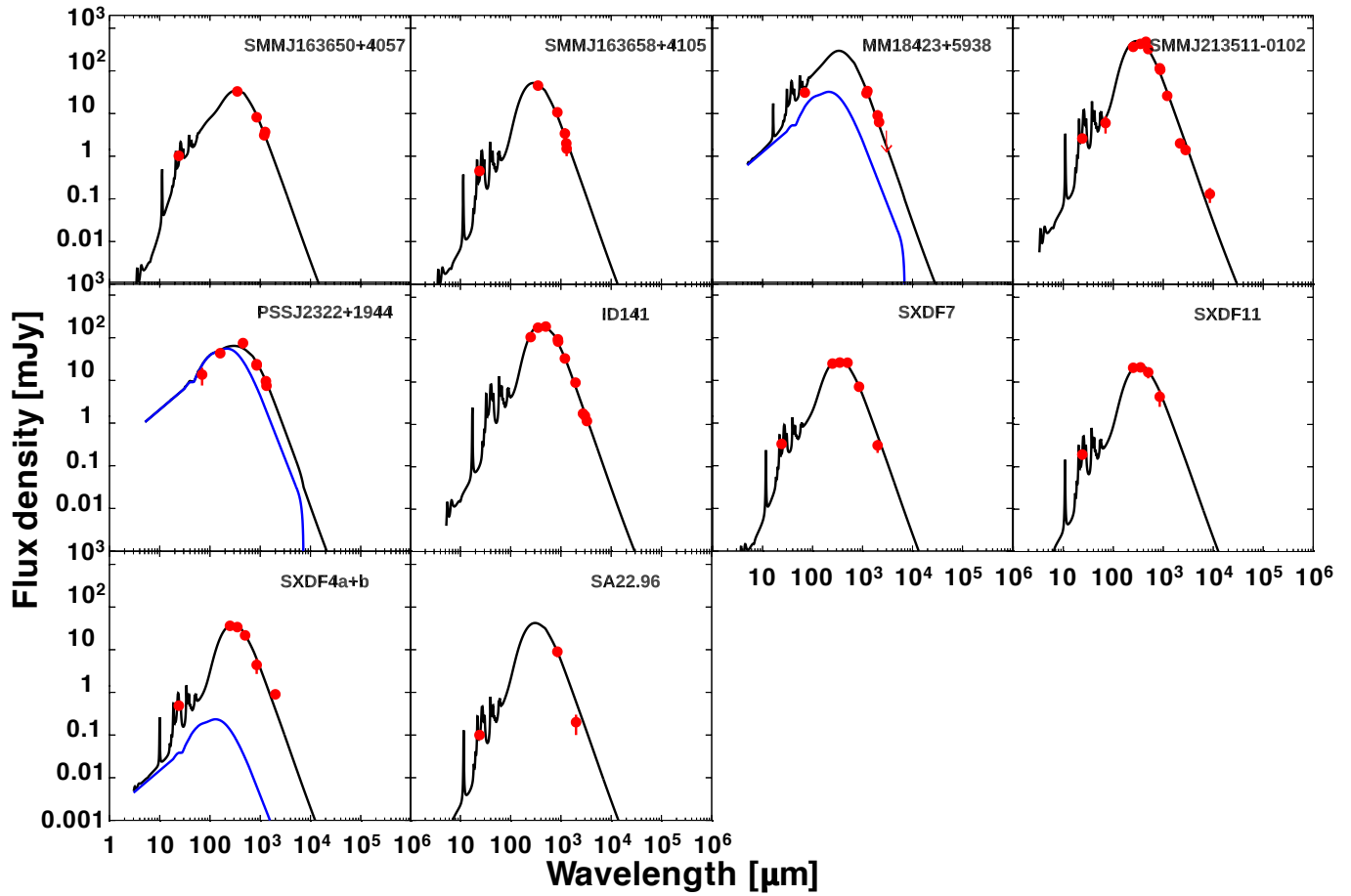


Figure 7. (continue)

(V18) cannot be captured by the fixed set of parameters in Kaufman et al. (1999).

We do not apply any more complex modeling to our compilation at this stage. Notably, we do not make such attempt for our main sequence galaxies at $z \sim 1$ due to the lack of constraining power in our observations. The LVG method would likely be able to capture both CO and [C I] at the same time (e.g., Israel et al. 2015), but it relies on the knowledge of both low- and high- J transitions, especially considering the growing evidence of the existence of a two-phase ISM, the hottest peaking even above $J_{\text{upper}} = 7$ (Liu et al. 2015; Yang et al. 2017; Cañameras et al. 2018). This information is not available for the vast majority of our sample of main sequence galaxies, following the general lack of constraints on the CO SLED of high-redshift normal galaxies (Daddi et al. 2015, Daddi et al. in preparation). We refer the reader to the original works producing such LVG modeling when accessible, mainly for lensed SMGs or very local objects. Similar considerations apply for the introduction of shock models. Moreover, spatially well resolved observations will be necessary to study the relative distributions of [C I] and CO and gauge, e.g., the effect of enhanced cosmic rays rates in high redshift galaxies, as unresolved or marginally resolved emission is dominated by the phases where both species are abundant (Papadopoulos et al. 2018). We also note that the observed ratios $L_{[\text{C I}]^3 P_2 - ^3 P_1} / L_{[\text{C I}]^3 P_1 - ^3 P_0} \lesssim 3.5$ in all but 3 objects are not compatible with extra heating from X-ray dominated regions (XDR) at the $n \sim 10^4 \text{ cm}^{-3}$ derived for the galaxies with both [C I] lines available (Meijerink et al. 2007; Nesvadba et al. 2018).

Table 5. Flux corrections for the ALMA observations of galaxies on the main sequence.

ID	Size	Flux increase		
	arcsec	[C I] $(^3P_1 - ^3P_0)$, CO (4-3)	CO (5-4)	CO (2-1)
(1)	(2)	(3)	(4)	(5)
4233	1.229 ± 0.279	–	–	–
7540	1.219 ± 0.322	–	–	–
13205	< 0.448	$< 5\%$	5%	9%
13250	0.907 ± 0.476	–	–	–
18538	0.514 ± 0.062	–	–	–
18911	< 1.248	31%	113%	39%
19021	0.184 ± 0.055	–	–	–
26925	1.239 ± 0.206	–	–	–
30694	0.691 ± 0.155	–	–	–
32394	1.572 ± 0.204	–	–	–
35349	0.859 ± 0.029	–	–	–
36053	< 0.578	$< 5\%$	28%	–
36945	< 0.595	$< 5\%$	$< 5\%$	11%
37250	0.893 ± 0.044	–	–	–
37508	< 0.208	$< 5\%$	$< 5\%$	$< 5\%$
38053	0.612 ± 0.239	–	–	–
44641	0.604 ± 0.190	–	–	–
121546	< 1.074	19%	–	–
188090	0.426 ± 0.015	–	–	–
192337	0.579 ± 0.026	–	–	–
208273	0.459 ± 0.048	–	–	–
218445	1.152 ± 0.347	–	–	–
256703	0.891 ± 0.030	–	–	–

NOTE—Column 1: ID. Column 2: Size in arcsec. Upper limits are at $< 1\sigma$. Column 3-5: Flux increase when extracting the source with a circular Gaussian (GILDAS/UV_FIT/C_GAUSS) with fixed FWHP = 1σ upper limit on the size, compared with the extraction with a point source profile (GILDAS/UV_FIT/POINT): $I_{\text{Gauss}}/I_{\text{Point}}$. Corrections below $< 5\%$ are not applied.

Table 6. Content of the data tables.

Name	Units	Description
ID	...	Source identifier
D	Mpc	Distance (for the local sample only)
z_{spec}	...	Spectroscopic redshift
μ (dust, gas)	...	Magnification factor for lensed sources (for the high-redshift sample only)
L_{IR}	L_{\odot}	Total IR luminosity integrated within $8 - 1000 \mu\text{m}$, corrected for the dusty torus emission if the galaxy is not AGN dominated
T_{dust}	K	Dust temperature from a optically thin modified black body model of the IR emission
L' (line)	$\text{K km s}^{-1} \text{pc}^2$	L' luminosities of the specified line
I (line)	Jy km s^{-1}	Velocity-integrated fluxes of the specified line
f_{AGN}	...	Fraction of IR emission due to dusty tori (for the high-redshift sample only)
Type	...	Galaxy type (MS=Main Sequence; SB=StarBurst; AGN/QSO=Active Galactic Nucleus/Quasar; for the high-redshift sample only)
AGN	...	Galaxy with AGN contamination and an entry in Véron-Cetty & Véron (2010) (for the local sample only)
Facility	...	Facility used to detect the [C I] line emission.
References	...	References to the original works presenting observations of each source.

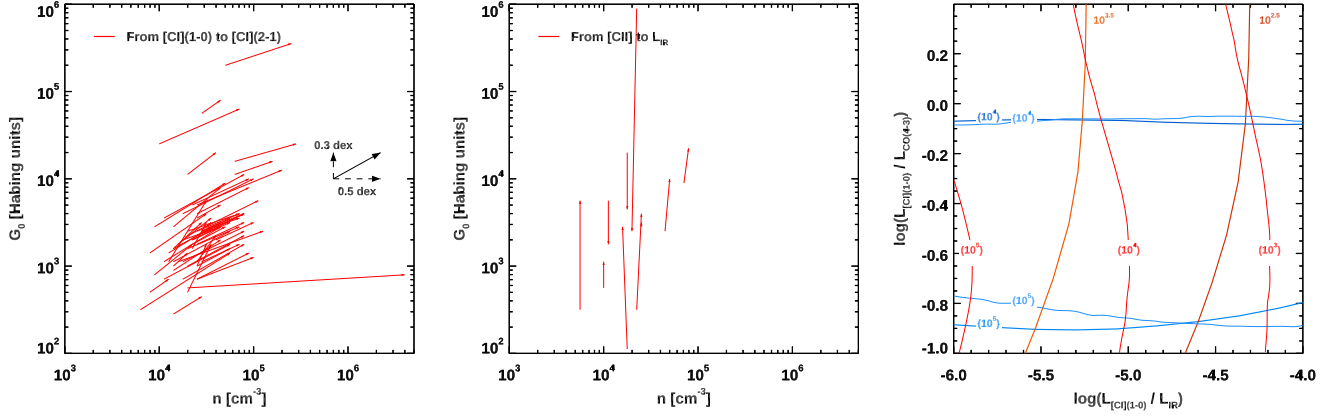


Figure 8. Test on [CI](${}^3P_2 - {}^3P_1$) vs [CI](${}^3P_1 - {}^3P_0$) and [CII] and comparison with previous modeling. *Left:* Best-fit gas density n [cm^{-3}] and intensity of the UV radiation field G_0 [Habing units] from PDR modeling by Kaufman et al. (1999) derived using [CI](${}^3P_1 - {}^3P_0$) or [CI](${}^3P_2 - {}^3P_1$) and keeping every other quantity fixed. Only galaxies with detections of both lines are shown. The red arrows map the difference in n, G_0 moving from [CI](${}^3P_1 - {}^3P_0$) to [CI](${}^3P_2 - {}^3P_1$) modeling. The black arrows indicate the average difference between the two estimates. *Center:* Best-fit n [cm^{-3}] and G_0 [Habing units] derived using the [CII] or L_{IR} as proxies of G_0 and keeping every other quantity fixed. Only galaxies with detections of both quantities are shown. The red arrows map the difference in n, G_0 moving from [CII] to L_{IR} modeling. *Right:* Blue and red lines respectively indicate the tracks of constant gas density n [cm^{-3}] and intensity of the UV radiation field G_0 [Habing units] in the [CI], CO ($4-3$), and L_{IR} plane of Figure 1. The tracks are computed from the PDR modeling by Kaufman et al. (1999). Thick darker lines show the modeling used in this work. Thin lighter lines mark the modeling adopted by Alaghband-Zadeh et al. (2013). The labels indicate the values corresponding to each track.

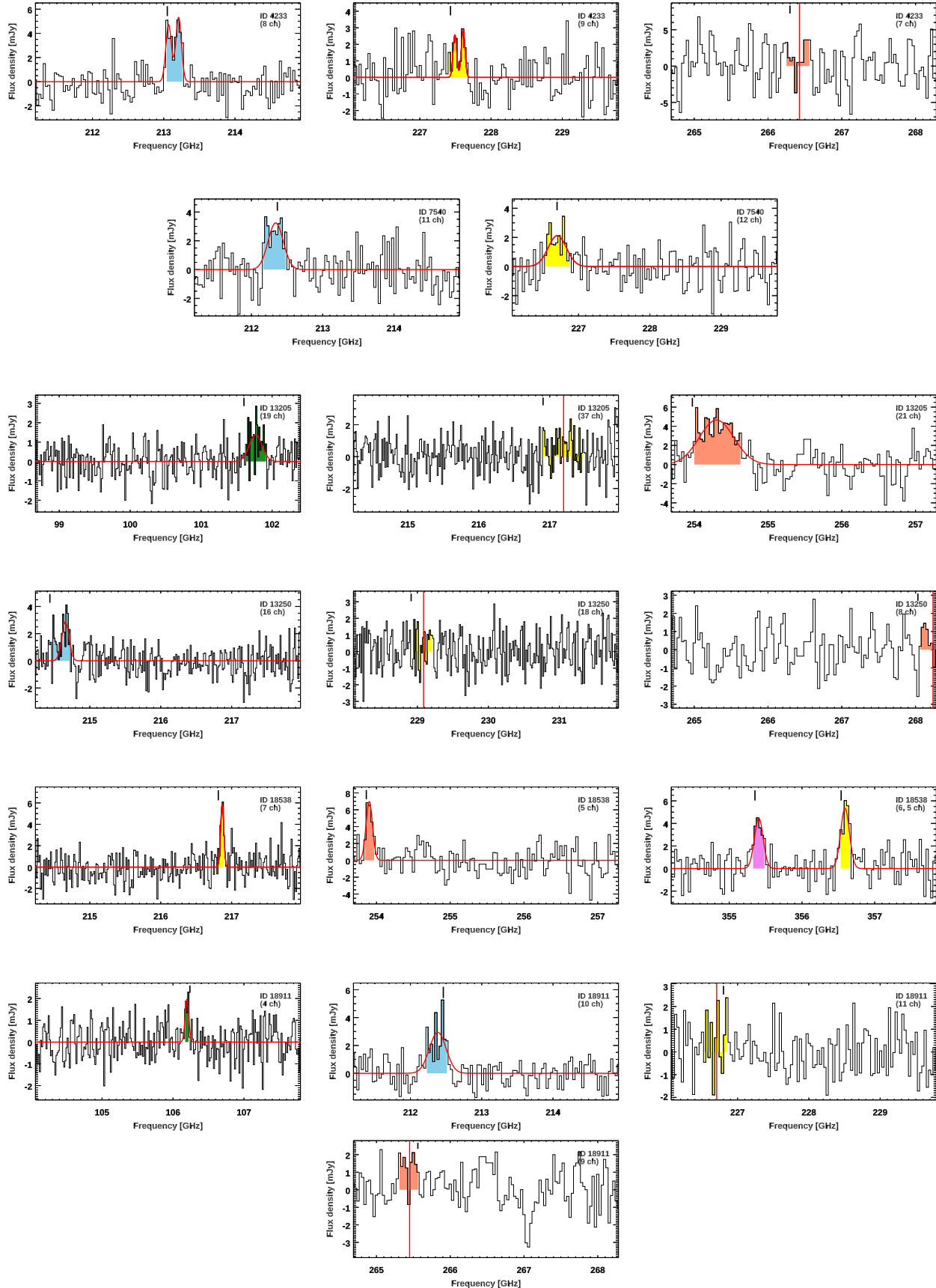


Figure 9. ALMA spectra covering multiple CO and [C I] lines for our sample of main sequence galaxies at $z \sim 1.2$ (see Appendix D for details).

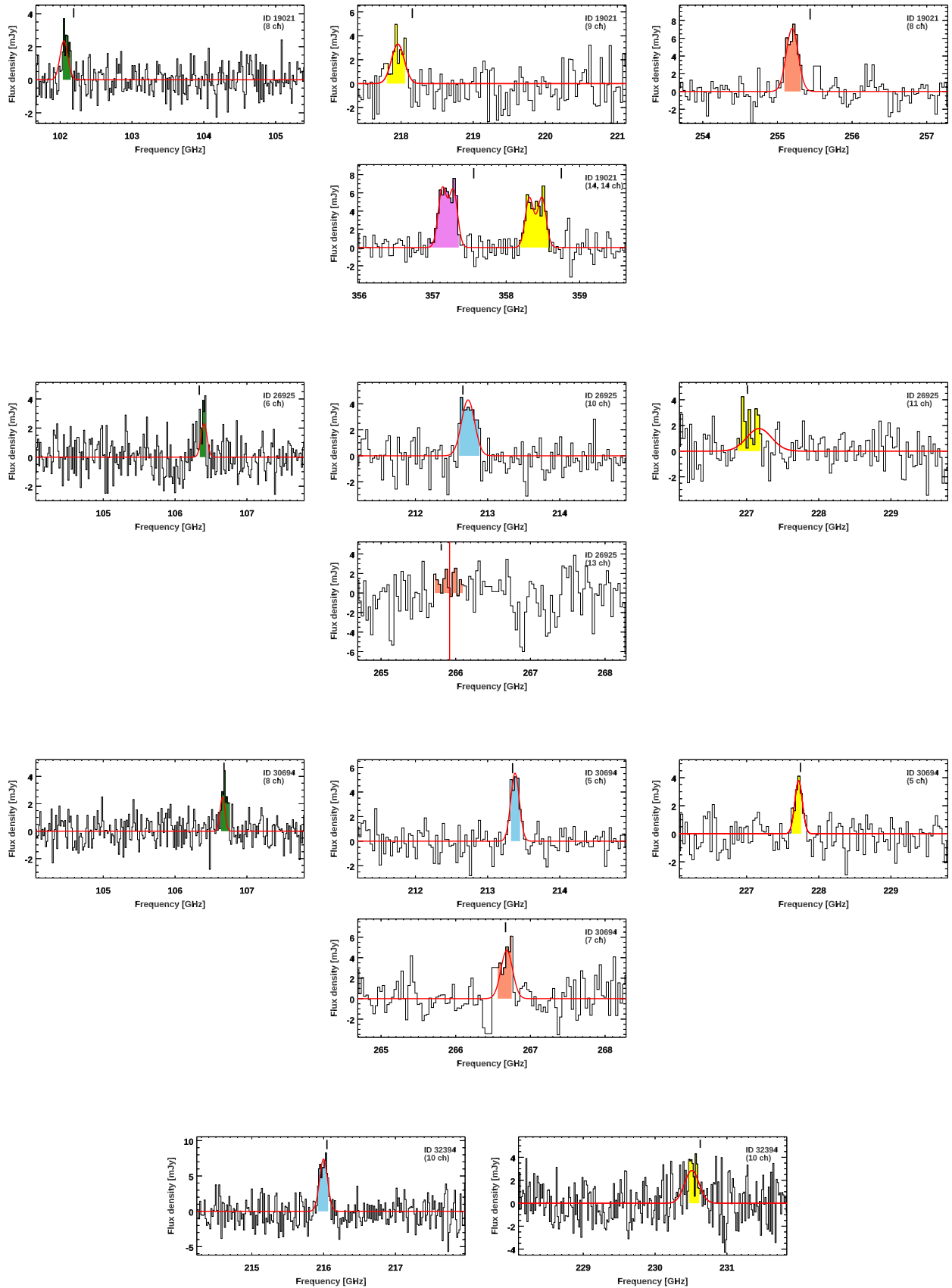


Figure 9. (continue)

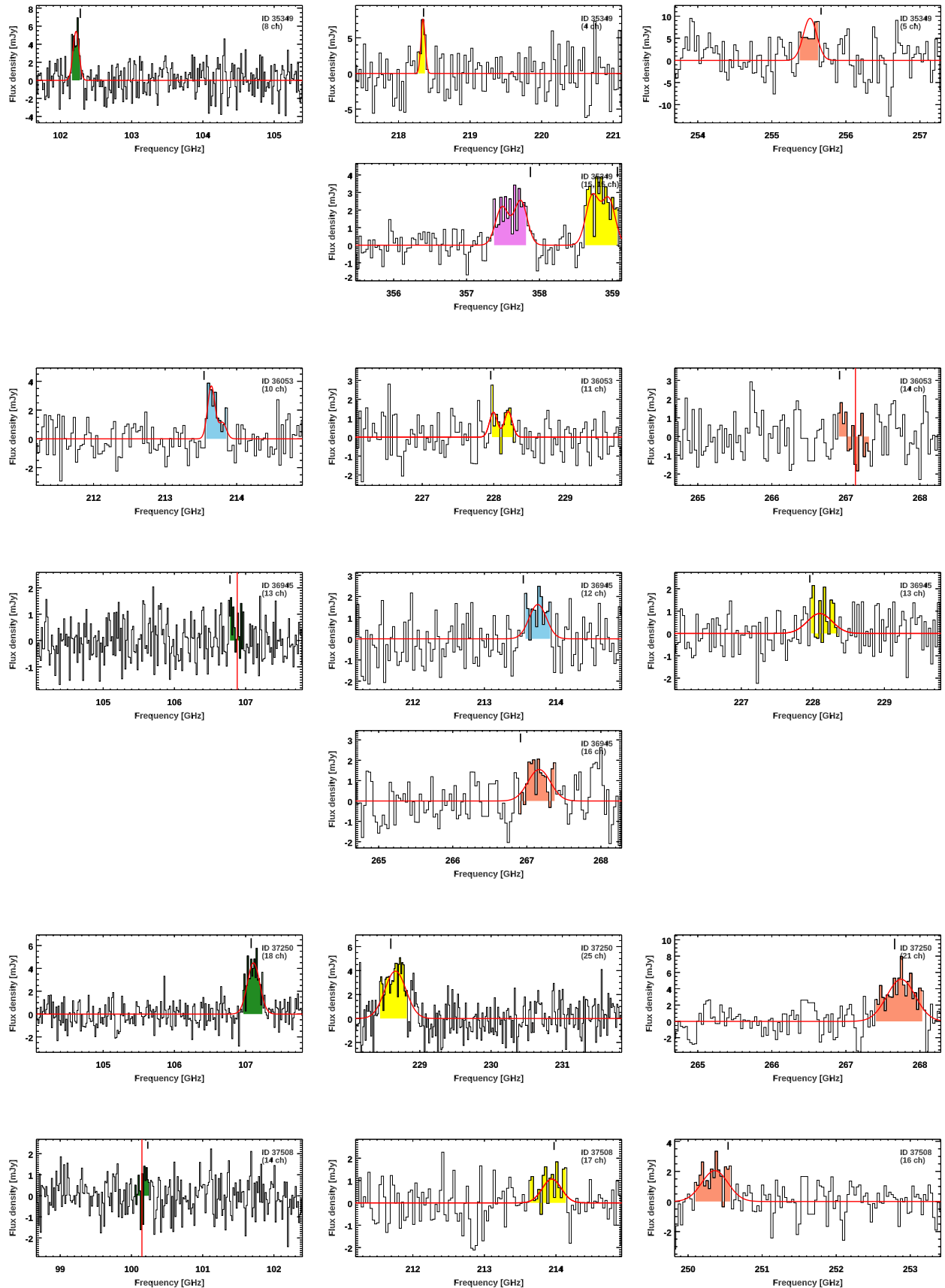


Figure 9. (continue)

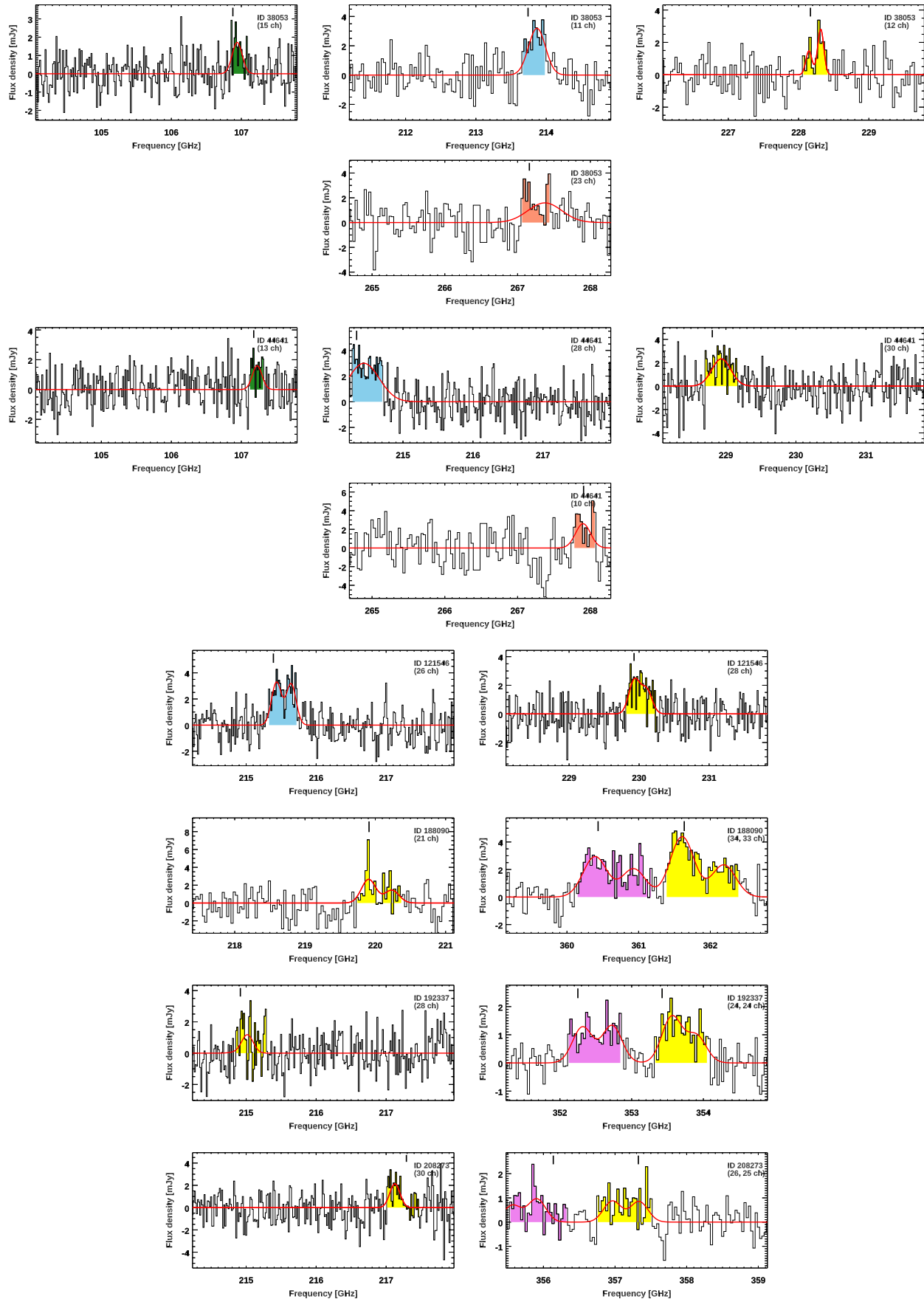


Figure 9. (continue)

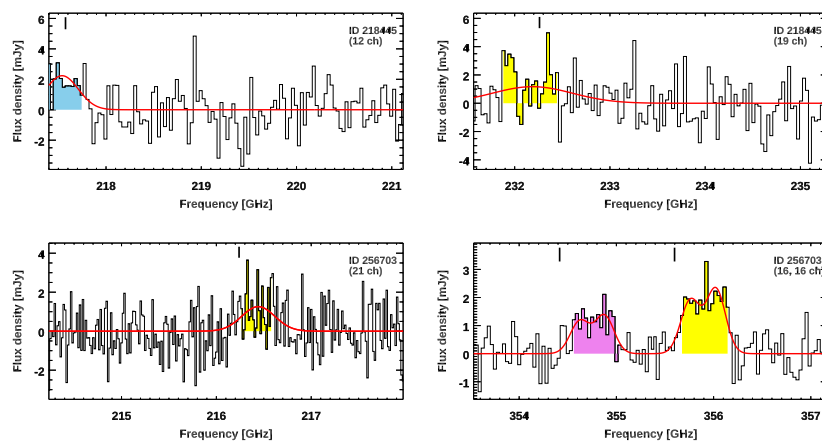


Figure 9. (continue)